AFRL-AFOSR-VA-TR-2019-0230

Novel Spatially and Temporally Resolved Meso-scale Experimental Quantification of Temperature and Deformation Fields in Heterogeneous Energetic Materials

Min Zhou
GEORGIA TECH RESEARCH CORPORATION

07/11/2019
Final Report

Air Force Research Laboratory
AF Office Of Scientific Research (AFOSR)/ RTA1
Arlington, Virginia 22203
Air Force Materiel Command

REPORT DOCUMENTATION PAGE

Form Approved
OMB No. 0704-0188

1. REPORT DATE *(DD-MM-YYYY)*	**2. REPORT TYPE**	**3. DATES COVERED** *(From - To)*
06/26/2019	Final technical report	9/30/2015 to 03/29/2019

4. TITLE AND SUBTITLE
Novel Spatially and Temporally Resolved Meso-scale Experimental Quantifcation of Temperature and Deformation Fields in Heterogeneous Energetic Materials

5a. CONTRACT NUMBER
A9550-15-1-0499

5b. GRANT NUMBER
A9550-15-1-0499

5c. PROGRAM ELEMENT NUMBER

6. AUTHOR(S)
Min Zhou, Georgia Institute of Technology
Naresh Thadhani, Georgia Institute of Technology
Daniel Eakins, Institute of Shock Physics, Imperial College London

5d. PROJECT NUMBER

5e. TASK NUMBER
1-4

5f. WORK UNIT NUMBER

7. PERFORMING ORGANIZATION NAME(S) AND ADDRESS(ES)
Georgia Institute of Technology, 801 Ferst Dr., School of Mechanical Engineering, Atlanta, GA 30332-0405

8. PERFORMING ORGANIZATION REPORT NUMBER
2506N64-002

9. SPONSORING/MONITORING AGENCY NAME(S) AND ADDRESS(ES)
Dr. Martin J. Schmidt, Air Force Office of Scientific Research (AFOSR), Dynamic Materials and Interactions Program Officer (PO), 875 North Randolph Street, Suite 3112
(703) 588-8436 (Office), Email: martin.schmidt@us.af.mil

10. SPONSOR/MONITOR'S ACRONYM(S)
AFOSR

11. SPONSOR/MONITOR'S REPORT NUMBER(S)

12. DISTRIBUTION/AVAILABILITY STATEMENT
Unclassified, Distribution A -- Approved for public release

13. SUPPLEMENTARY NOTES

14. ABSTRACT
This project focused on (1) the development of a computational capability for analyzing the response of energetic materials such as PBX and GX under dynamic loading and (2) establishment of the ignition behavior of heterogeneous energetic composites as microstructure at the microscale. The thermal-mechanical computational framework (CODEX, Cohesive Dynamics for Explosives) utilizes a fully dynamic cohesive finite element method (CFEM) which allows the effects of large deformation, thermomechanical coupling, failure in the form of microcracks, and frictional heating to be tracked. The capabilities resulting from this project can be used to design new energetic materials of interest to the USAF.

15. SUBJECT TERMS

16. SECURITY CLASSIFICATION OF:			**17. LIMITATION OF ABSTRACT**	**18. NUMBER OF PAGES**	**19a. NAME OF RESPONSIBLE PERSON**
a. REPORT	**b. ABSTRACT**	**c. THIS PAGE**			**19b. TELEPHONE NUMBER** *(Include area code)*

Novel Spatially and Temporally Resolved Meso-scale Experimental Quantification of Temperature and Deformation Fields in Heterogeneous Energetic Materials

Grant # FA9550-15-1-0499

Final Report on 6/26/2019, for period 9/30/2015 to 03/29/2019

Submitted to

Dr. Martin J. Schmidt

Dynamic Materials and Interactions Program
Air Force Office of Scientific Research (AFOSR)
875 North Randolph Street, Suite 3112
(703) 588-8436 (Office), Email: martin.schmidt@us.af.mil

by

Min Zhou
The Woodruff School of Mechanical Engineering &
The School of Materials Science and Engineering
Georgia Institute of Technology
Atlanta, GA 30332-0405
Tel: 404-894-3294, Fax: 404-894-0186
min.zhou@gatech.edu

Naresh Thadhani
School of Materials Science and Engineering &
School of Mechanical Engineering
Georgia Institute of Technology
Atlanta, GA 30332
Tel: 404.894.2651, Fax: 404-894-9140
naresh.thadhani@mse.gatech.edu

Daniel Eakins
Institute of Shock Physics**,** Imperial College London**,**
+44 (0) 20 7594 5982, London SW7 2AZ**,** U.K.
d.eakins@imperial.ac.uk

Abstract

The deformation, failure, and heating in heterogeneous energetic materials (HEM) determine their mechanical, thermal, and reaction responses under dynamic conditions. There is a lack of experimental capabilities for quantifying the processes at the microstructure levels. The objectives of this project are to develop novel experimental capabilities for obtaining time- and space-resolved measurements of the temperature, deformation and stress conditions in these heterogeneous energetic materials (HEM). The specific diagnostics developed include

(1) A novel first-time ever experimental capability for directly measuring the spatial distribution and temporal evolution of microstructure-level temperature and deformation fields;
(2) Simultaneous velocity/stress and time-resolved spectroscopy using multilayer optical microcavity structures for monitoring evolving heterogeneities during shock loading; and
(3) Reflectance-change-based active lighting technique for recording of temperature fields.

In this report, we discuss the achievements in these three areas made through this project. We focus on both the capabilities developed and results obtained. Publications and presentations are also summarized.

1. Simultaneous high-speed IR and VL imaging (GT)

This is a novel and brand new capability that was conceived and developed in this project. To establish the capability for simultaneously obtaining time-resolved and space-resolved measurements of the deformation fields and temperature fields with microsecond-level time resolutions and micron-level space resolutions, we have integrated a state-of-the-art high-speed infrared (IR) camera and a high-speed visible light (VL) camera in a split-Hopkinson pressure bar (SHPB) or Kolsky bar apparatus.

1.1. Experimental Layout

For simultaneous capturing of deformation and temperature fields, the visible (VL) and infrared (IR) emissions from the sample passing through the sapphire window are separated by a dichroic beam splitter, as illustrated in Fig. 1. The beam splitter reflects over 85% of VL light and directs the light into the VL camera which is mounted vertically. Coincidentally, the beam splitter transmits over 85% of the IR emission, which passes through a set of custom-designed correction lenses and then goes into the IR camera mounted horizontally. The VL images are captured by the high-speed camera which has a framing rate of 100,000 fps, a spatial resolution of 7.04 μm, and a field of view (FOV) of 2.8 mm × 3.2 mm to record the deformation of the sample. The IR camera operates at 5,000 fps with a 13.24 μm spatial resolution and a 2.5 mm × 2 mm FOV. The IR and VL cameras are synchronized in time and calibrated in spatial positions, consequently, the VL and IR images can be coordinated for extraction of the deformation and temperature fields. Illustrations and pictures of the experimental setup are shown in Figs. 1 and 2, respectively.

A Phantom v2512 camera, which can operate at 25,700 fps at 1 Megapixel resolution and 1,000,000

fps at 128 × 32 pixels, is used to record the VL images. An Infinity microscope lens is used along with the VL camera to zoom in far enough to capture high-resolution meso-scale images. Selecting a proper light source for high-speed imaging in this experimental layout is difficult. On one hand, a powerful light source is necessary at framing rates around 100,000 fps, such light sources require significant space. On the other hand, the VL lens is very close to the confinement box and sample (< 2 inches), leaving only very tight space for a light source. A powerful light source close to the sample may also affect the temperature measurement because of the heat from the light source. To overcome these challenges, two LED light sources along with fiber optics are used. The LED light sources are placed far from the sample and the light is projected onto the sample through optical fibers, as shown in Fig 2. This configuration minimizes heating relative to other light sources such as halogen lights and permits proper placement within the tight space of the experimental setup. Tests show that this lighting approach does not affect the temperature measurements.

A Fast-IR 2K camera (Telops Inc. in Quebec, Canada) is used to record the IR images. This camera operates at 2,000 fps with a spatial resolution of 320 ×240 pixels and 90,000 fps with a spatial resolution of 64 × 64 pixels. The IR camera is calibrated along with the corrective IR lenses and the beam splitter.

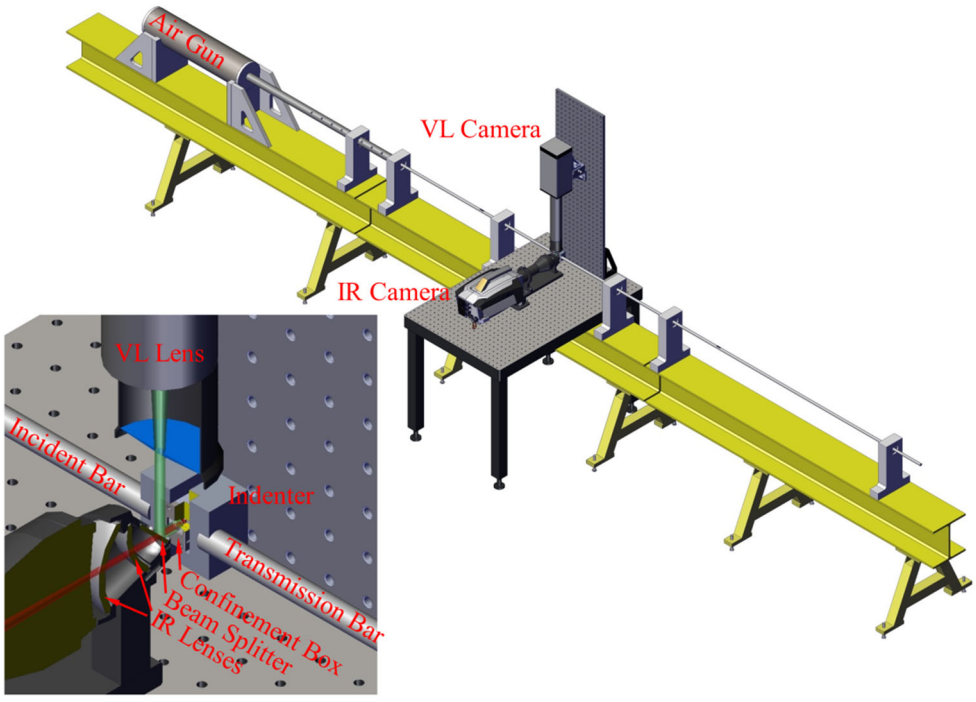

Figure 1. Experimental setup for simultaneous high-speed IR and VL imaging.

A triggering system is designed and built to operate the two cameras simultaneously. Two sets of sensors are placed close to the incident bar to detect the motion of the bar and trigger the cameras and other instrument, via a control box. The control box also activates electric solenoid valves to fire an air gun to start the experiment and secure the loading mechanism.

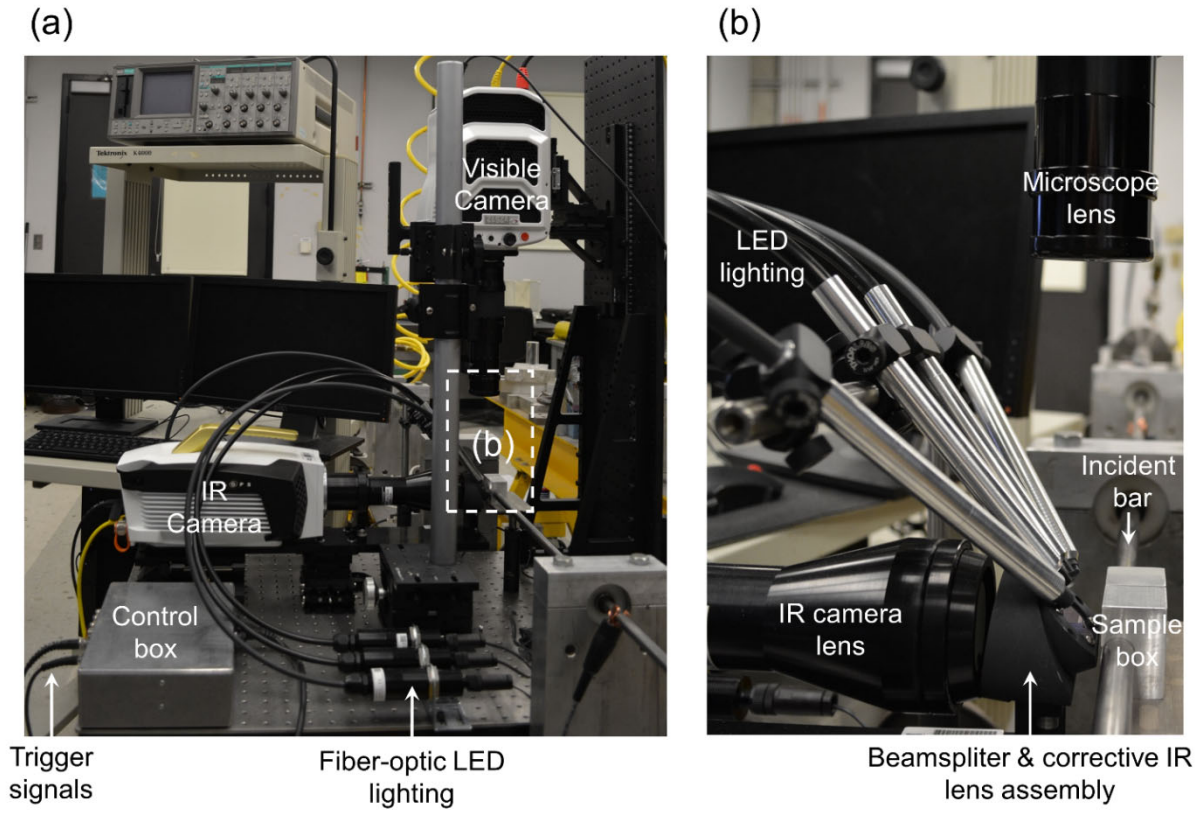

Figure 2. Pictures of the experimental system. (a) An overall view of the components, (b) a close-up view of the dichroic beam splitter and the VL and IR lenses.

Since the IR camera is calibrated to blackbody emission, the camera reading must be calibrated using the emissivity of the sample's constituents in order to arrive at the correct temperature field. The emissivity of the sample material (sugar) is determined to be ~0.95 by calibrating the camera reading to the initial (known) temperature of the sample. The calibration is based on the Stefan-Boltzmann law in the form of

$$E = e\,\sigma\,T_s^4, \tag{1.1}$$

where E is the power flux recorded by the IR camera, e is the emissivity of the sample material, σ is the Stefan–Boltzmann constant, and T_s is the temperature of the sample. Since the IR camera is calibrated to blackbody radiation, the relation between the camera's temperature reading T_c and the sample temperature T_s is $\sigma T_c^4 = e\,\sigma\,T_s^4$, yielding

$$T_s = \frac{T_c}{\sqrt[4]{e}}. \tag{1.2}$$

This analysis assumes the emissivity remains constant during the deformation. It is believed that changes in the emissivity over the ranges of temperature and deformation are relatively small. However, more accurate determination of the emissivity and emissivity changes will be carried out in the future. The emissivity *e* is determined for the following materials: sucrose (0.97), sugar (0.97), a polymer composite as a simulant for energetic materials (0.97), and steel indentors use in the experiments (0.81).

1.2. Experiments

The experiments focused on granular sugar, sucrose, and a polymer composite as simulants of heterogeneous energetic materials. Here, we focus on granular sugar and sucrose. To obtain overall compressive loading, the sample is confined in a box with a sapphire window and loaded between two indenters via a pair of indenters, as illustrated in Fig. 3. The internal dimensions of the sample chamber are 3×3×2.2 mm. The confinement box is designed such that the ends of the incident bar and the transmission bar are placed inside indenters. This design prevents lateral movements of the confinement box and the sample for proper imaging. Figure 3(b) illustrates the relative positions of the confinement box, the incident bar, and the transmission bar. The preparation of the samples include initial gentle compression to achieve different packing densities and characterization of the samples.

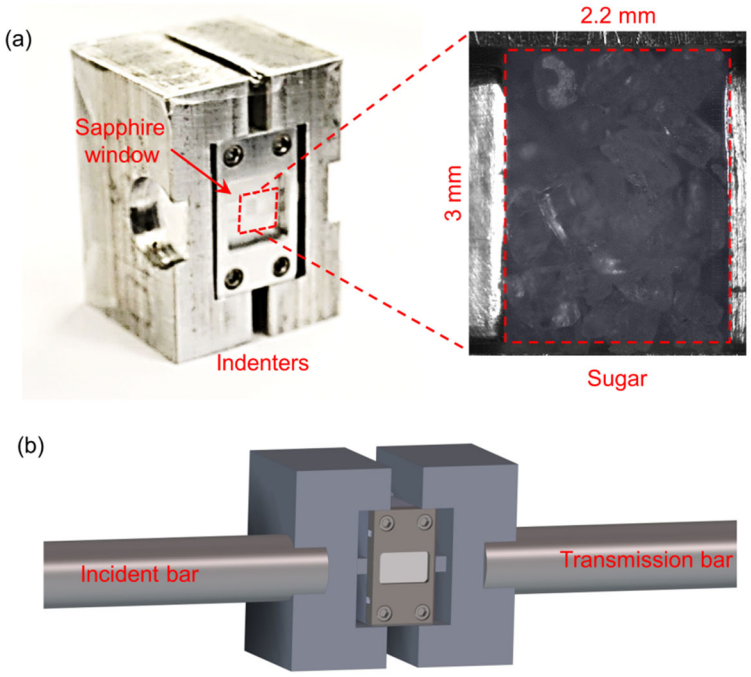

Figure 3. (a) The confinement box and the sample, and (b) relative positions of the confinement box, the incident bar, and the transmission bar.

The compressive loading (horizontal direction in Fig. 3(b)) causes densification, crashing and granular flow of the grains in the sample, leading to temperature increases. Figure 4 shows a sequence of images recorded as the VL camera. Four stages of deformation are seen, including (1) densification

and grain crushing $(40 < t \le 200\ \mu s)$, (2) bulk compression $(200 < t \le 360\ \mu s)$, (3) unloading due to rebound of the incident bar in the SHPB apparatus $(360 < t \le 400\ \mu s)$, and (4) recompression $(400 < t \le 800\ \mu s)$. The initial structure of the sample's grains can be seen in Figure 4(a). The histories of the overall (global) true strain and true strain rate for this experiment are shown in Figure 5.

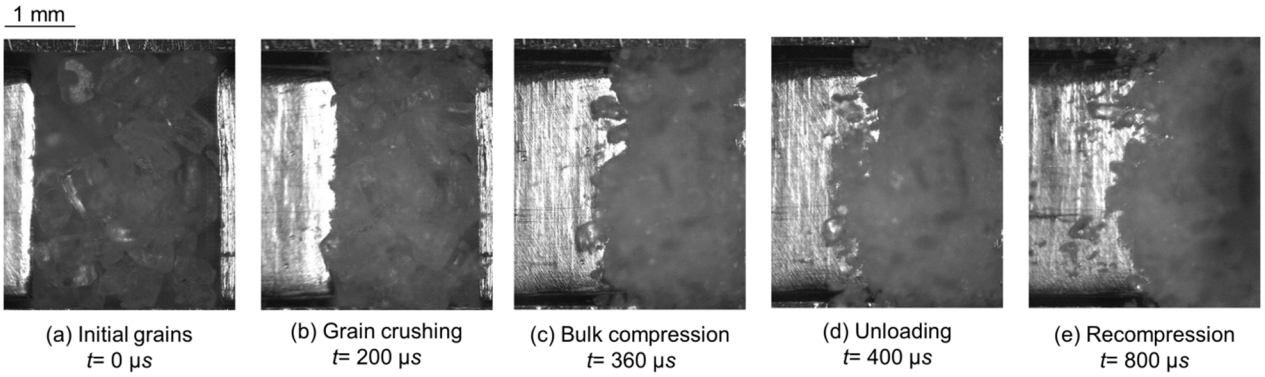

Figure 4. Configurations of the sample at different stages of deformation, (a) initial state at t=0 μs, (b) end of the grain crushing stage $(40 < t \le 200\ \mu s)$, (c) bulk compression $(200 < t \le 360\ \mu s)$, (d) unloading $(360 < t \le 400\ \mu s)$, and (e) recompression $(400 < t \le 800\ \mu s)$.

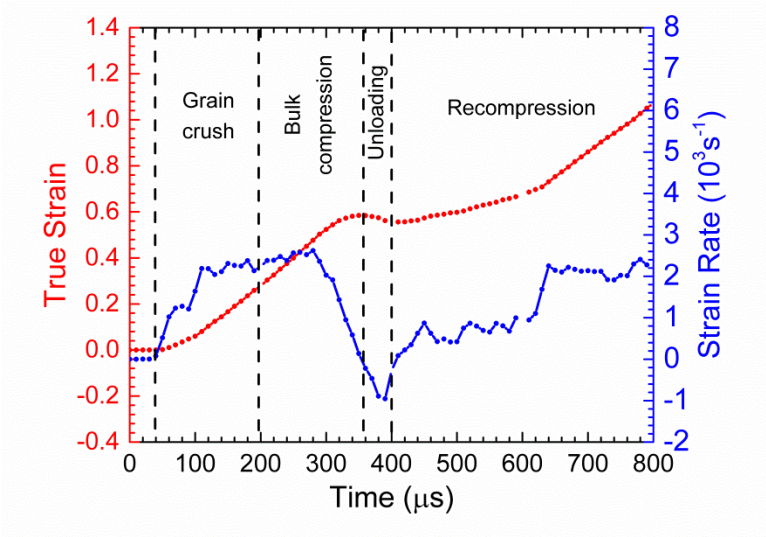

Figure 5. The histories of the overall (global) true strain and true strain rate for the experiment in Figure 4.

Figure 6 shows the distributions of the components of the Almansi strain rate and the temperature at four different times during the above experiment. The strain rate fields indicate highly heterogeneous deformation in the material. The normal strain rates show regions of instantaneous expansion and contraction in both axial directions. The shear strain rate show vertices or shear is both the clockwise and counterclockwise directions. These features are consistent with the flow of the granular the material. The next step of the analysis is to relate the deformation fields to the microstructure of the

material and ascertain how the grains and grain boundaries affect the deformation. The initial temperature of the sample at the beginning of loading is 290 K. The temperature increases to over 360 K as the deformation progresses, as seen in Fig. 6(b). Figure 7 quantifies size and temperature of the hotspots seen in these temperature fields. The number of hotspots at the four times is summarized in Fig. 7(a). The maximum equivalent hotspot diameter with each given temperature at the four times is shown in Fig. 7(b). Overall, more hotspots with higher temperatures are seen at the end of stage 4, after significant volumetric compression of the sample occurs in various stages of deformation. A stage-to-stage comparison offers more insight. Specifically, heating is minimal during the grain fracture/crushing in stage 1. Significant heating occurs during the overall compression in stage 2. The rebound and overall expansion in stage 3 causes the temperature in the hotspots to decrease due to heat conduction. The intense recompression in stage 4 causes both the temperature and size of the hotspots to increase. Overall, the inelastic deformation and friction associated with the granular flow during the bulk compression of the sample, rather than grain fracture, cause most of the heating. From $t = 400\ \mu s \quad (\varepsilon = 0.55)$ to $t = 600\ \mu s \quad (\varepsilon = 0.67)$, the sample does not undergo significant compression (Fig. 5). The lack of internal friction and constituent inelasticity in this period causes the number, size, and temperature of the hotspots to decrease (Fig. 7).

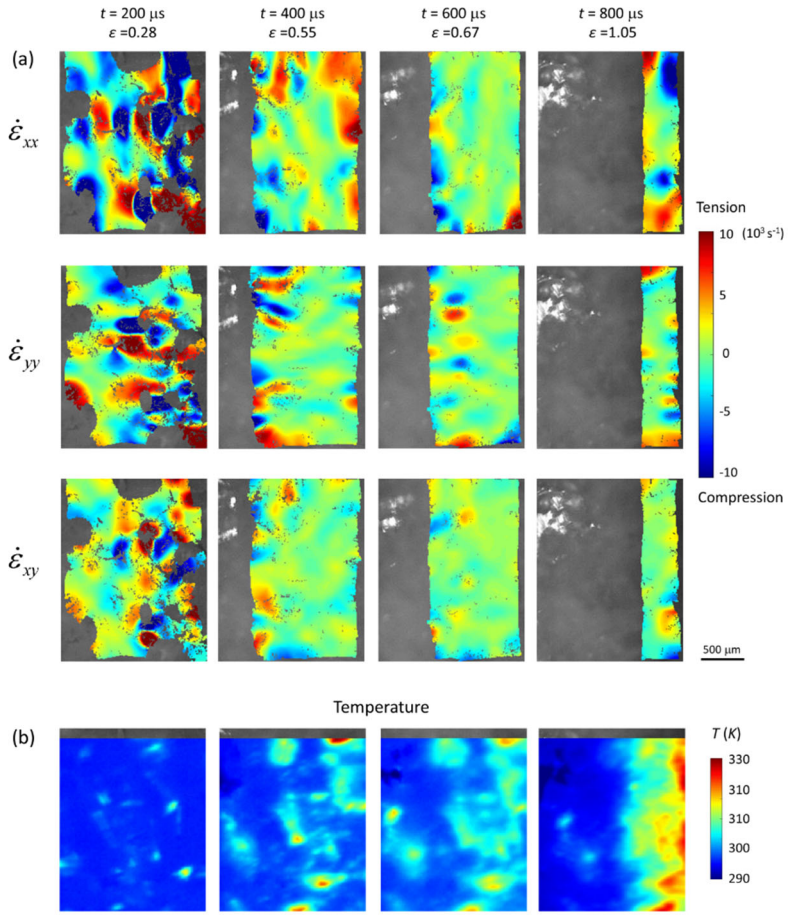

Figure 6. (a) Almansi strain rates of the sugar sample at t=200, 400, 600, and 800 µs, and (b) corresponding temperature distributions in the sample recorded by the IR camera.

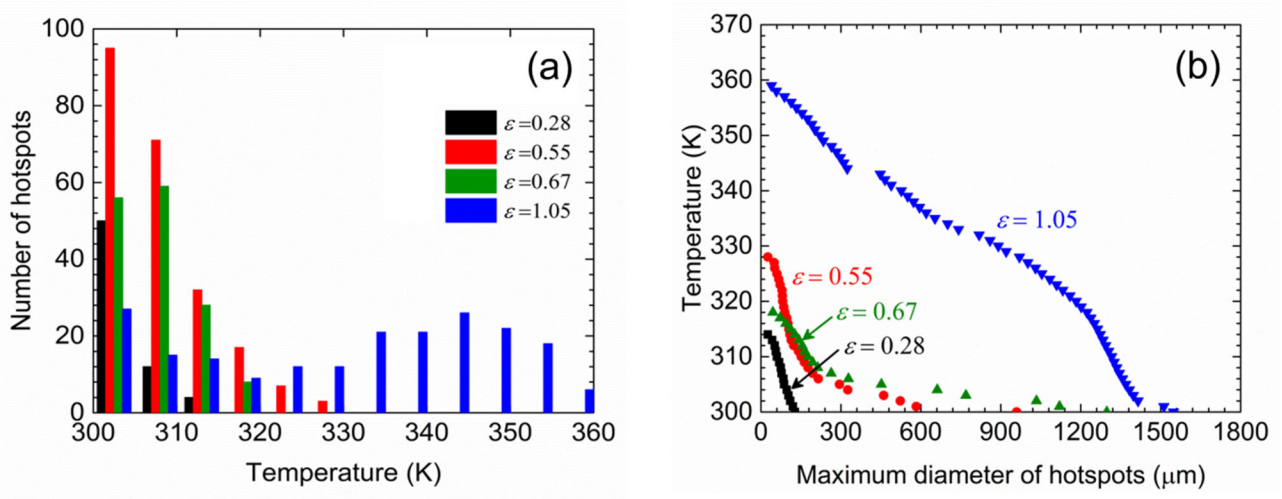

Figure 7. Quantification of hotspot in the temperature fields in Fig. 6, (a) number of hotspots at given temperature levels, and (b) maximum equivalent diameter of hotspot(s) with internal temperature levels at or above given levels.

Another set of experiments are conducted on sucrose $\left(C_{12}H_{22}O_{11}\right)$ granules with the molecular weight of 342.3 g/mol. The sucrose was purchased from Research Products International (RPI). The sucrose granules are graded using standard AASHTO sieves and three sets of samples with the average grain sizes of 165 μm, 362.5 μm, and 775 μm are selected for the experiments (Fig. 8). Figure 8 shows the initial density and average grain size of the three sets. During the experiments, the environment temperature and humidity were 296.3 ± 0.25 K and 42.9 ± 0.8 %, respectively. The deformation of the sucrose granules is crystallographically dependent. The elastic modulus of sucrose single crystals on the (100) crystallographic plane is 38 GPa and the modulus on the (001) plane is 33 GPa. The onset of shear stress causing plastic deformation in sucrose grains is 1 GPa [1].

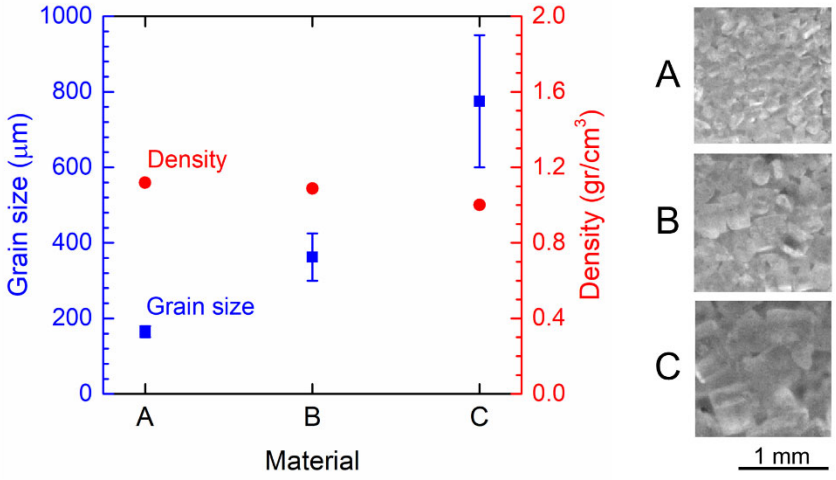

Figure 8. Grain size and density of materials.

The materials are confined in the sample box and compressed between the two indenters as the gas gun is fired. Under compression, the sucrose grains are fractured and smaller crushed particles hold together and form a coherent compact, which is known as the briquetting process. Sucrose has a high level of briquetting tendency under compression unlike other organic materials such as coal and sodium chloride [2]. Figure 9 shows an SEM image of material C $\left(\overline{d}_0 = 775\ \mu\text{m}\right)$ after the experiment. This figure shows that some grains have sizes similar to the initial grains, suggesting that these grains experience minor crushing under loading. In addition, Fig. 9 provides visual evidence of briquetting in the materials. Micro-squashing is important for achieving sufficient areas of contact between the particles in a compact in order for the whole sample to remain coherent after the pressure is released (i.e., briquetting). Although organic particles such as sodium chloride, coal, and sucrose are known to be brittle [3], these materials behave plastically if they are small and subjected to high levels of stress [4]. The critical size of particles for transition from fragmentation to plastic deformation is uncertain and varies over a considerable range of factors.

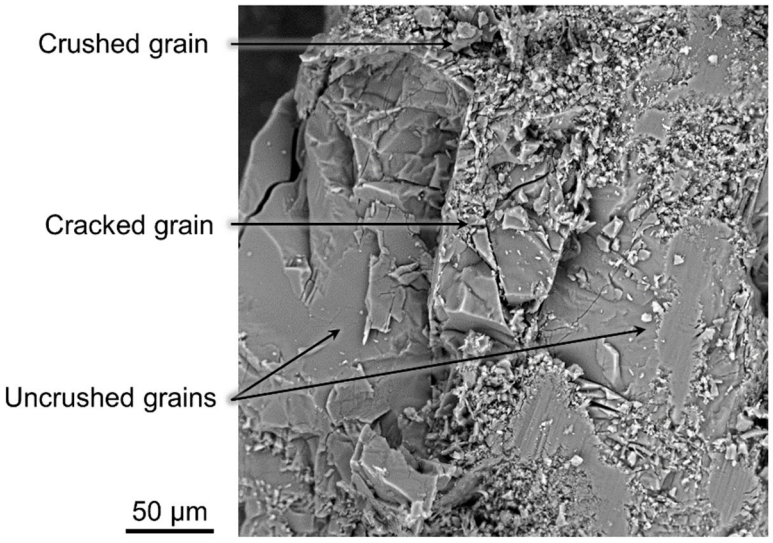

Figure 9. An SEM image of material C after the test.

Figure 10 shows the overall deformation (engineering strain, $\Delta L/L_0$, where $L_0 = 5$ mm is the initial length of the sample along the loading direction) in the materials as a function of time during the experiments. This figure shows three stages of loading; (1) fragmentation of grains $\left(0 \le t < 0.56\ \text{ms}\right)$, (2) briquetting $\left(0.56 \le t < 1.12\ \text{ms}\right)$, and (3) unloading $\left(t \ge 1.12\ \text{ms}\right)$. We calculated the overall strain according to relative position of indenters from visible images. The three materials show similar deformation trends during loading; therefore, we mainly discuss material C in this section. Figure 10 also specifies the times of infrared images, which are captured at every twenty visible images according to the framing rates of the two cameras. In addition, this figure differentiates between infrared images with and without temperature increase. Figure 11 shows the visible images and temperatures fields of the material during the experiment. The first infrared image showing temperature increase in the sample is captured at $t = 0.8$ ms, which occurs in the second stage of deformation.

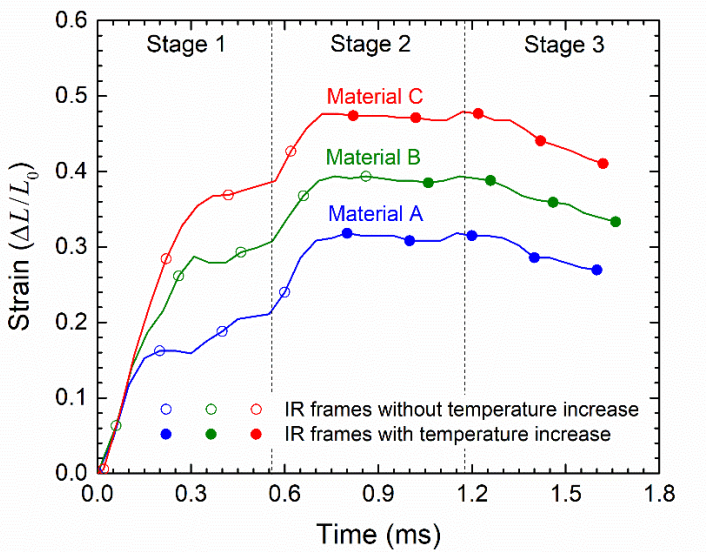

Figure 10. The overall strain in the materials as a function of time. The solid and hollow circles show the temperature frames with and without temperature increase.

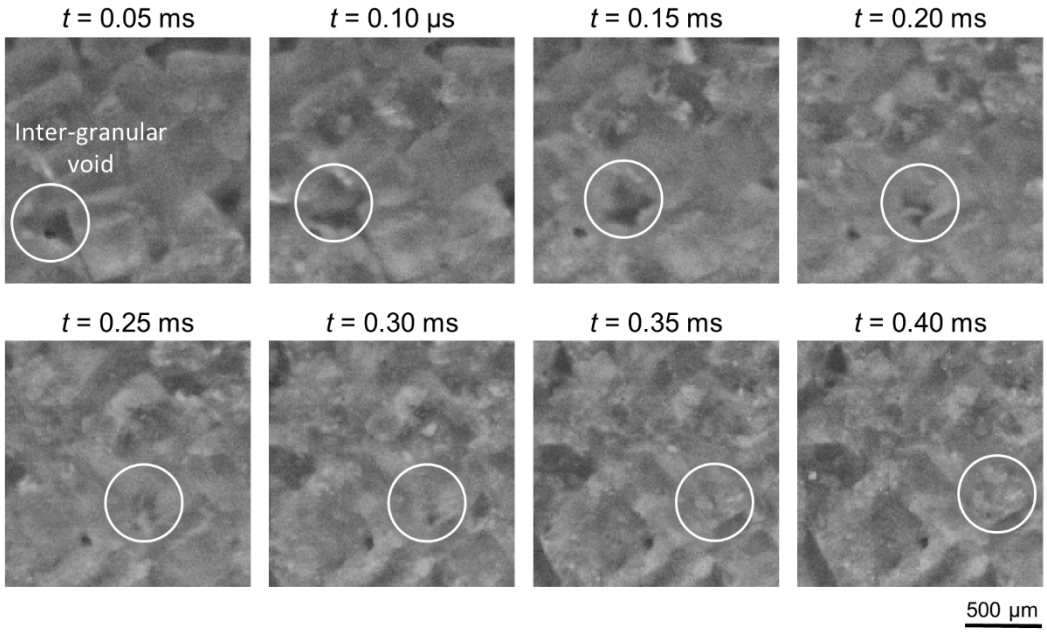

Figure 11. Visible image sequences of inter-granular void collapse (material C).

In the first stage of deformation $(0 \le t < 0.56 \text{ ms})$, material C (sieve 30) is compressed by 38% and inter-granular voids collapse as shown in Fig 10. Fine grains $(d \le 50 \text{ μm})$ resulting from fragmentations flow between large grains $(d \ge 250 \text{ μm})$ and fill the voids between them. The filled voids do not experience as extensive deformation as unfilled voids. In this stage, the IR camera captured two infrared images except the initial image $(t = 0)$ and none of them shows temperature

level increases. In the second stage of deformation $\left(0.56 \le t < 1.12 \text{ ms}\right)$, the material is further compressed by 10% and unlike in the first stage, a limited level of fragmentation is observed. Four IR images are captured in the second stage and the latter two images show increases in temperature levels inside the material. In the last stage $\left(t \ge 1.12 \text{ ms}\right)$, the material is partially unloaded as the overall strain decreases from 47.1% to 41.2%. The two IR images associated with the third stage show significant temperature increase in the material.

The two major heating mechanisms in the materials are plastic deformation and friction. Sucrose is known as brittle in general, but it can behave plastically if its grains are small and are subjected to high levels of stress. According to our observations, the grain fragmentation in the first stage does not directly contribute to heat generation in the materials; however, fragmentation affects heat generation by facilitating and enabling inelastic deformation and, more importantly, localized frictional heating along fragmented faces. Experimentally, it is challenging to quantify the contributions of these mechanisms in the formation of hotspots in materials. The developed experimental environment provides simultaneous visible and infrared images with high spatial resolution, which determines the locations of hotspots with respect to microstructure. The localized temperature spikes or hotspots are responsible for thermal softening, thermal runaway, and ignition in energetic materials. The perception of the locations of hotspots is critical for understanding the underlying mechanisms leading to formation of the hotspots. For example, a hotspot inside a grain and far from internal boundaries most likely results from inelastic deformation, while a hotspot at a boundary likely results from frictional dissipation at the boundary. In addition, knowledge of the potential locations of hotspots can be used to modify the local thermo-mechanical response of materials by changing the constituent and interfacial properties.

Figures 12 (a) and (b) show the sequence of visible images and the corresponding temperature fields of material C during the experiment, respectively. Due to highly non-uniform stress distributions in granular materials, some grains are negligibly loaded and fragmented during the loading event. As a result, there are a few large grains $\left(d \ge 250 \text{ μm}\right)$ in the formed briquette. Sucrose particles do not undergo plastic deformation until they are micro-squashed. Therefore, unfragmented or partially fragmented grains during experiments do not undergo plastic deformation and they only experience frictional dissipation at their boundaries. The boundaries of unfragmented grains are the primary locations of hotspots as shown in Fig. 12(b), suggesting the role of friction in the formation of hotspots.

Variations in the grain size of the materials provide perturbations to thermo-mechanical processes, causing temperature distributions to differ. Figure 13 shows temperature distributions in the three materials at $t = 1.23$ ms. Despite higher overall temperature levels, the temperature fields in the materials with smaller grain sizes (materials A and B) are less localized. Materials with smaller grains experience more energy dissipation, since smaller grains are more likely to undergo plastic deformation and their high surface to volume ratios facilitate frictional dissipation. As a result, the sucrose materials with smaller initial grain sizes generate higher amount of heat under loading, and their overall temperatures are higher than those in the materials with larger initial grain sizes. Despite more overall heat generation, the materials with smaller grains have lower levels of peak temperatures. This reduction in localized heating results from two factors. First, energy dissipation resulting from plastic deformation spreads more widely in the material and is less localized. Second,

frictional heating in the materials with smaller grains spreads more widely since the density of friction sites increases significantly. Figures 14 (a) and (b) show the average temperature and the peak temperature levels of the materials, showing that materials with larger grain sizes have lower average temperatures but higher peak temperatures. Specifically, the difference between the average and peak temperatures in material A $\left(\bar{d}_0 = 165\ \mu\text{m}\right)$ is only 1.3 K, while the difference in material C $\left(\bar{d}_0 = 775\ \mu\text{m}\right)$ is 16.5 K. The correlation between local deformation and temperature in hotspots is discussed in the next section.

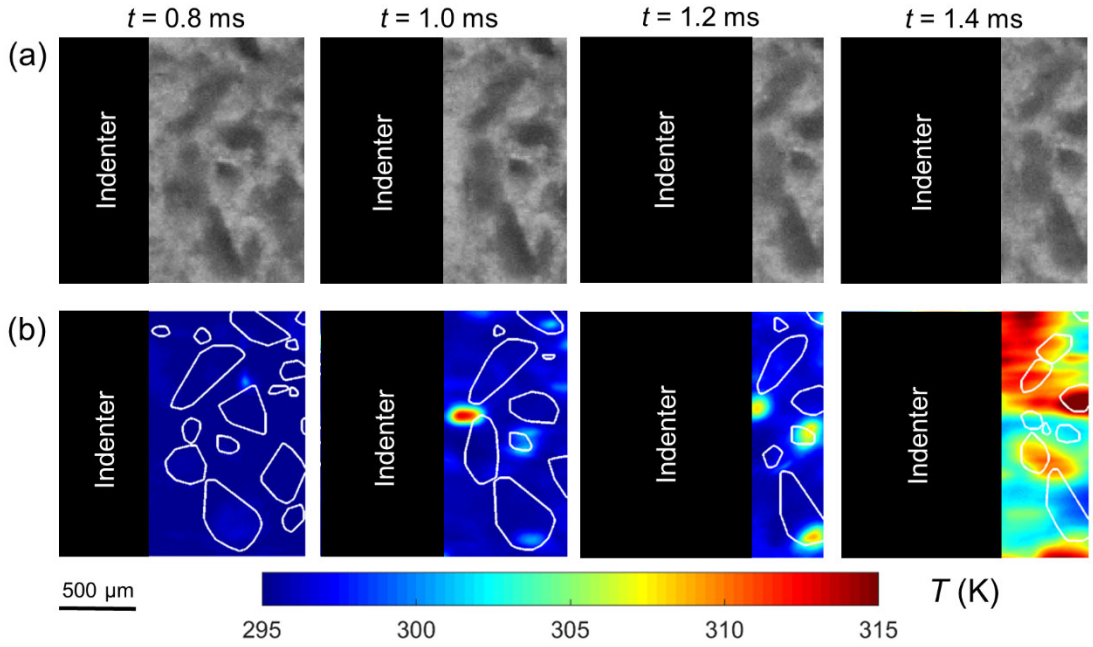

Figure 12. Visible and infrared image sequence of the material C. The temperature level in the material does not temperature increase for $t < 0.8$ ms.

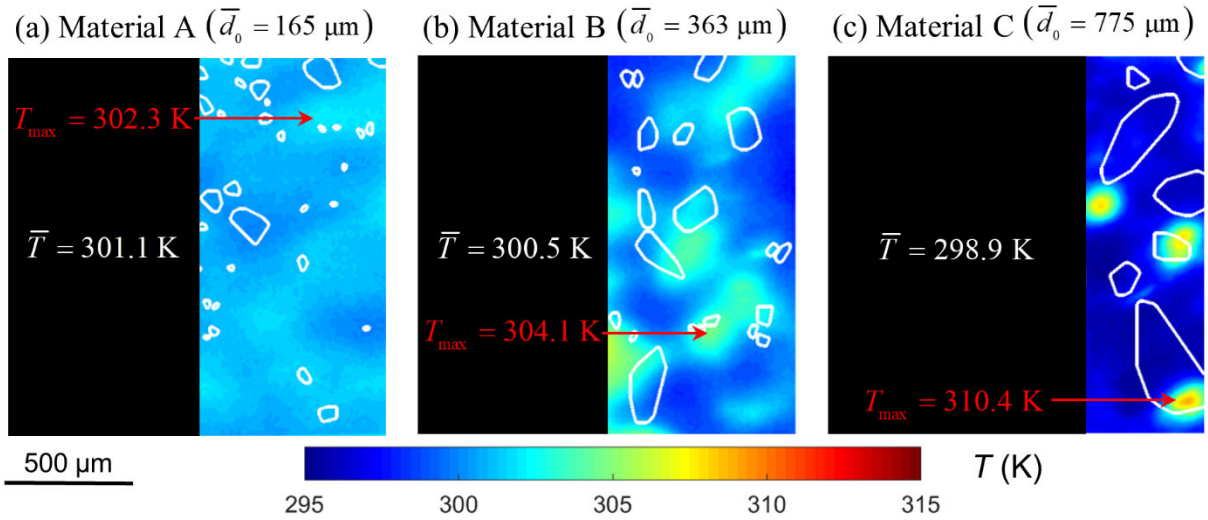

Figure 13. Temperature fields in the materials at $t = 1.23$ ms; (a) material A, (b) material B, and (c) material C.

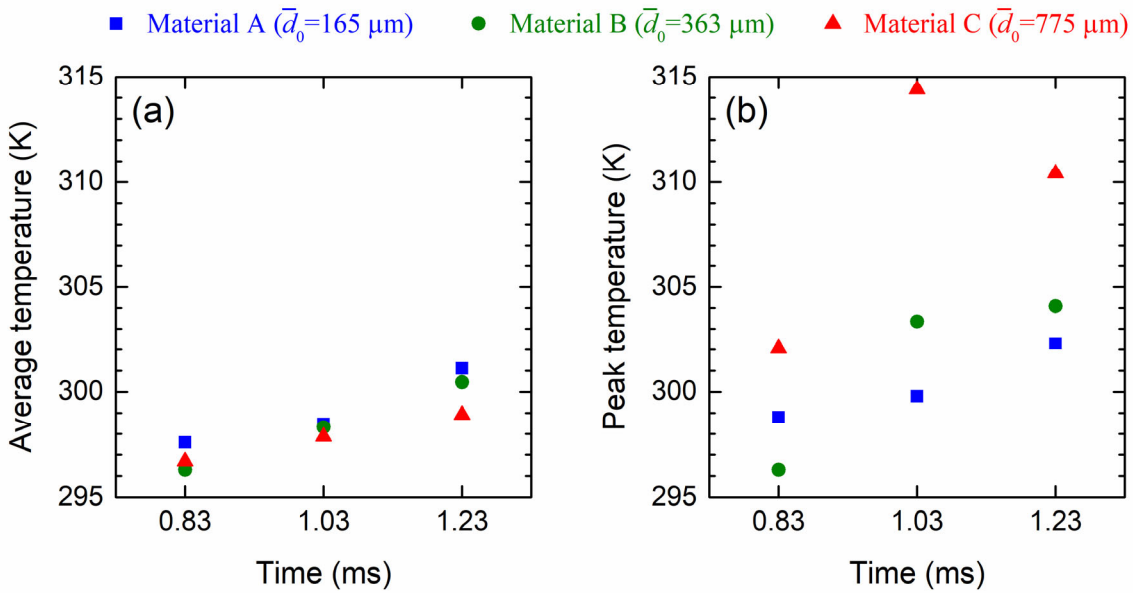

Figure 14. (a) Average temperature levels in the materials, and (b) peak temperature levels in the materials.

Hotspots result from various deformation mechanisms; therefore, deformation fields are critical in determination of dominant mechanisms contributing to formation of hotspots. To obtain deformation fields, we performed the digital image correlation (DIC) analysis, which is an important and widely used non-contact technique for measuring material deformation. We used the Ncorr software package, which is an open-source subset-based 2D DIC package that amalgamates modern DIC algorithms proposed in the literature with additional enhancements [5]. Due to uncertainties in the correlation between current and reference images as a result of significant fragmentations in the first stage, the DIC analysis is only performed for the second stage of deformation. Since the temperature of the material does not increase until the latter part of the second stage of deformation, the deformation mechanisms involved in the second stage are dominant for the temperature increase in the material. Figure 15 shows the temperature fields and the corresponding strain fields for material C at the second stage of deformation. The strain fields indicate highly heterogeneous deformation in the material. The normal strains show regions of instantaneous expansion and contraction in both axial directions. The shear strains show vertices or shear in both the clockwise and counterclockwise directions. These features are consistent with the flow of granular materials. Figure 16(a) quantifies the size and number of hotspots whose interior temperatures are above or at temperature T in Fig. 15(b). Figure 16(b) quantifies the deformation modes (volumetric and maximum shear strains) for the hotspots presented in Fig. 16(a). The two major heating mechanisms in the materials are plastic deformation and friction, both of which result from shear deformation beyond certain limits. Experimentally, it is challenging to quantify the contribution of each mechanism in the formation of hotspots in materials. Both volumetric and maximum shear strain levels are higher in the hotspots with higher temperatures and the shear deformation is locally dominant in the hotspots. The results show a direct correlation between maximum shear strain and temperature levels in hotspots.

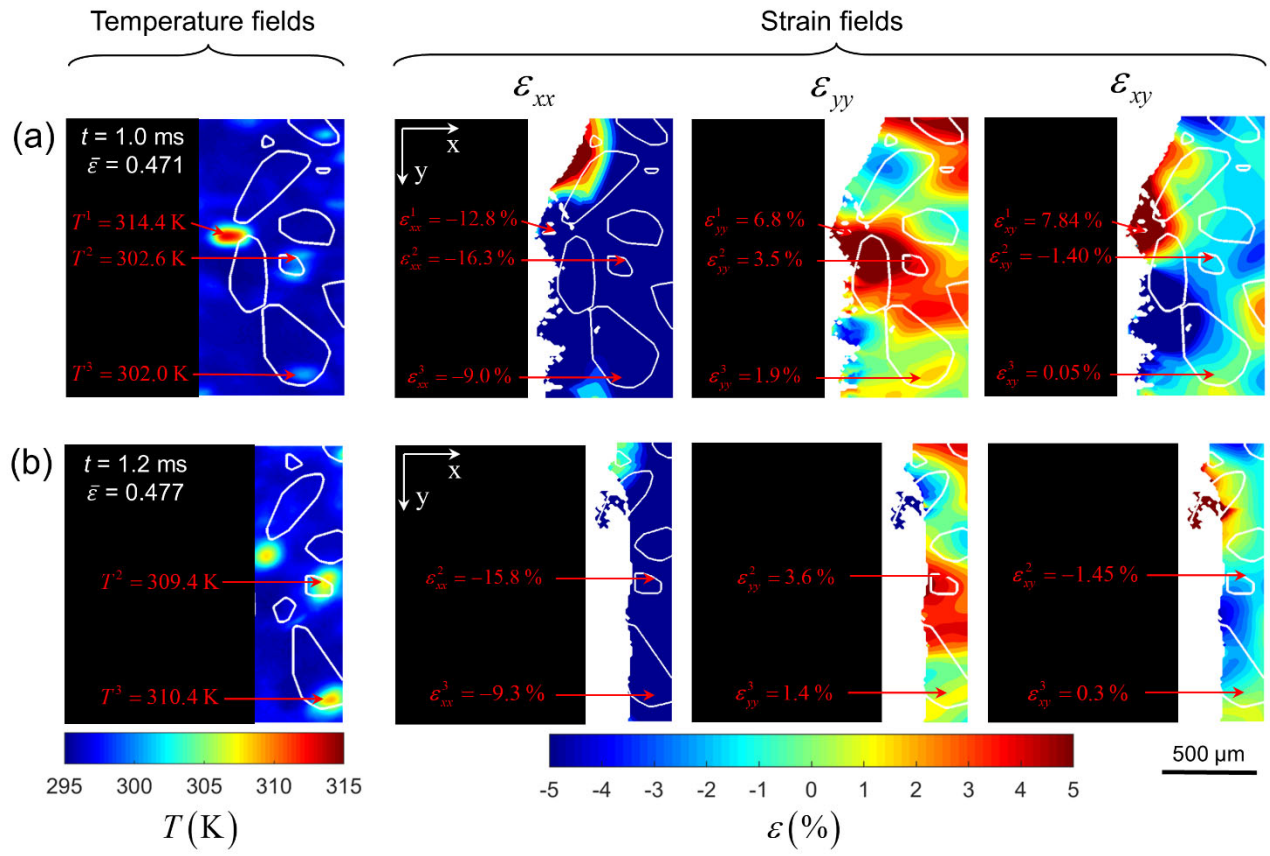

Figure 15. Temperature and strain fields of the material C; (a) $t = 1.0$ ms, and (b) $t = 1.2$ ms.

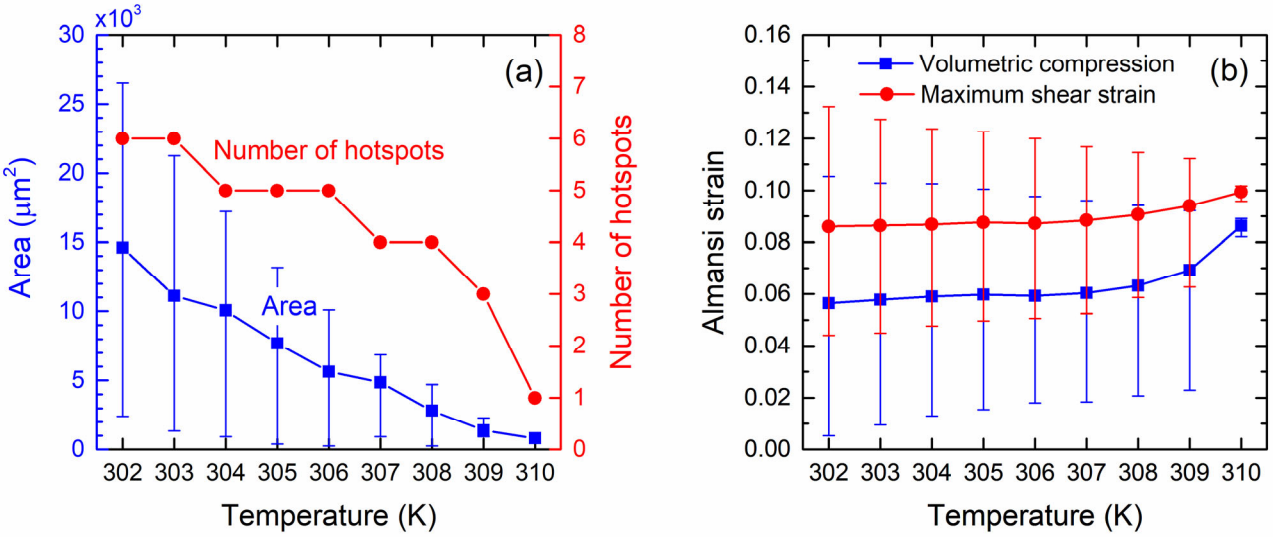

Figure 16. (a) Hotspots characteristics (size and temperature), and (b) local volumetric and maximum shear Almansi strains in hotspots as a function of the hotspot temperature for material C at $t = 1.23$ ms.

Proper selection of subset size relative to the length-scale of physical features is important in DIC analyses. Smaller subsets yield better resolutions for small-scale features while larger subsets cause more averaging and may be appropriate for larger-scale features. Results obtained from smaller subsets contain higher levels of noise that may obscure small-scale physical features. Large subsets reduce noise levels but may not allow capture of small-scale physics. In addition, a subset needs to be large enough to track an arrangement of speckles/features in order to perform correlation. In the experiments here, the natural pattern of the briquetted sample is used for the DIC analysis. To compensate for the lack of a speckle pattern, the subset needs to be large enough to capture boundaries of grains in order to calculate the deformation fields inside grains. Therefore, a large circular subset with a diameter of 0.67 mm (50 pixels) that circumscribes the largest grain in the sample is used.

Hotspots are important physical features in the experiments performed here. Hotspot 2 (labeled with T^2 in Fig. 15) is at the boundary of a small grain with a size of 0.173 mm next to another grain with a size of 0.3 mm. Therefore, a good correlation can be achieved even with subset sizes smaller than 0.67 mm (50 pixels) for the neighborhood of hotspot 2. Figure 17 shows the strain components associated with hotspot 2 at $t = 1.0$ and 1.2 ms for subset sizes $0.4 - 0.94$ mm $(30 - 70$ pixels$)$. The smallest subset with a size of 0.4 mm (30 pixels) yields the highest level of ε_{xy} but the lowest levels of ε_{xx} and ε_{yy} in hotspot 2. As the subset size increases to 0.94 mm (70 pixels), ε_{xy} decreases and the normal strains $(\text{i.e., } \varepsilon_{xx} \text{ and } \varepsilon_{yy})$ reach constant levels. The increase in ε_{xy} with decreasing the subset size shows that the shear deformation is more localized. Since this localized deformation occurred at a grain boundary, this shear deformation results from friction. This observation is consistent with what we see in our recent computational study [6]. In addition, the increase in ε_{xy} associated with the 6.4 K increase in the temperature of hotspot 2 from $t = 1.0$ ms to $t = 1.2$ ms is perspicuous with small subsets. Specifically, the increase in ε_{xy} from $t = 1.0$ ms to $t = 1.2$ ms is 1.4% for the subset size of 0.4 mm (30 pixels) while the increase is only 0.1% for the subset size of 0.64 mm (50 pixels).

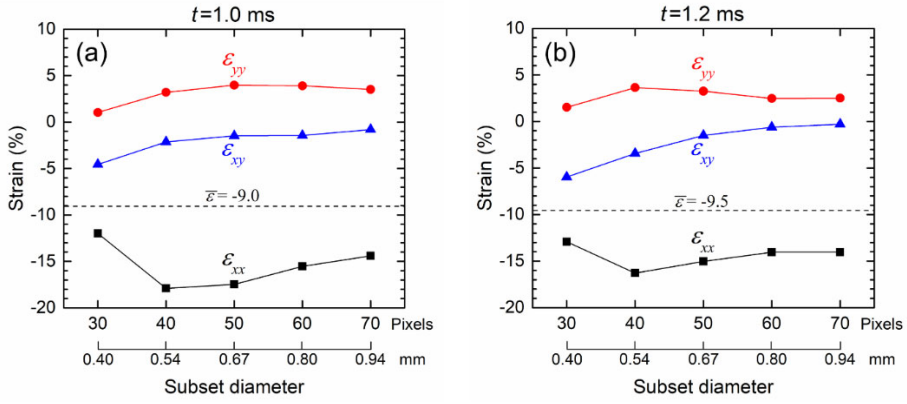

Figure 17. Variations in local strains (ε_{xx}, ε_{yy}, and ε_{xy}) inside hotspot 2 (labeled with T^2 in Fig. 16) during the second stage of deformation as a function of subset size; (a) $t = 1.0$ ms, and (b) $t = 1.2$ ms. Here, $\bar{\varepsilon}$ denotes the overall strain occurred in the sample during the second stage of deformation.

Summary

We have developed the first-ever novel capability **MINTED** (**m**icroscale **in**-situ imaging of **te**mperature and **d**eformation fields under dynamic loading) for time-resolved and space-resolved measurements of the temperature and deformation fields at the microstructure level for dynamic conditions is developed. The method cohesively integrates a state-of-the-art high-speed infrared (IR) camera and a high-speed visible light (VL) camera in a split-Hopkinson pressure bar (SHPB) or Kolsky bar apparatus. To simultaneously capture deformation and temperature fields at normal incidence, the visible (VL) and infrared (IR) emissions from the sample are separated by a dichroic beam splitter. The beam splitter reflects VL light and directs the light into the VL camera. This is a general capability that can be used to study deformation, failure and heating in a range of materials, including metals, composites, ceramics, soft materials, and energetic materials.

To demonstrate the capabilities of the MINTED system, we performed experiments on sucrose granules, which are widely used as a simulant of energetic crystals. The experiments involve three sucrose materials with the average grain sizes of 165 μm, 362.5 μm, and 775 μm. The samples are confined in a box behind a sapphire window. Under loading, the grains are fragmented, squashed, and briquetted. The materials undergo significant temperature increases in the briquetting stage. Despite higher overall temperature levels, the temperature fields in the materials with smaller grain sizes are less localized. The unique capability here for simultaneous measurements of deformation and temperature fields allows the determination and tracing of the locations of hotspots or material points with respect to the material microstructure features. The results show that the boundaries of unfragmented grains are the primary locations of hotspots. The maximum shear strain levels are locally higher than volumetric strain levels in the hotspots, and there is a direct correlation between maximum shear strain and temperature levels in hotspots.

2. Simultaneous Velocity/Stress & Time-resolved Spectroscopy using Multilayer Optical Microcavity Structures for Monitoring Evolving Heterogeneities during Shock Loading (GT)

Objective and Approach

The overall objective of our project is to combine velocity (point/line VISAR) interferometry measurements with time-resolved spectroscopy using recently developed Optical Microcavity (OMC) structures to monitor evolving heterogeneities and their localized stress, strain, and thermal effects during dynamic laser-shock loading of heterogeneous materials. OMCs create supported spectral modes with low reflectivity, which manifest with wavelength shifts due to externally induced changes as a function of cavity thickness and refractive index.

Optical Microcavity (OMC) structures are composed of a dielectric material cavity layer sandwiched between two metal mirror layers. OMCs are essentially one-dimensional optical resonators, composed of a central resonating cavity surrounded by reflective surfaces. OMCs utilize a resonant cavity mode at a specific and narrow range of wavelengths to produce high transmission and low reflectivity band centered at the characteristic wavelength λ_0 which is a function of the cavity thickness and its refractive index. Under mechanical loading, the response of the structure is,

governed by its constitutive response with total strain determined by the applied stress, strain rate, temperature, thermal expansion and stress-optic effect, which in turn is a function of the refractive index and its dependence on thermos-optic effects. With dynamic loading, the hydrodynamic equation of state (EOS) response of the material, shock-induced temperature changes, and variations in refractive index (related to density according to the Gladstone-Dale relation) can further influence the induced spectral response, but can be accounted to obtain clearly resolvable spectral shifts as a function of the magnitude of dynamic loading [7].

Design Methodology and Fabrication of OMC Structures

During the course of the past year, we have investigated various OMC designs consisting of two Ag mirror layers and cavity layers composed of either SiO_2, Al_2O_3, of PMMA. We investigated a simple SiO_2 and Al_2O_3 OMC design consisting of three layers: two Ag mirror layers and a cavity layer shown in Fig. 18 along with their respective reflectance spectra of simulated designs, using experimental data from the fabricated structures. The two different optical microcavity structures were designed and fabricated; the first using SiO_2 (n=~1.46) as the cavity material and another with Al_2O_3 (n=~1.77) as the cavity layer. OMCs were designed using OpenFilters to have a sharp transmission peak around 590 nm for optimum spectral sensitivity and fabricated using fabrication techniques such as e-beam evaporation, and ion-assisted deposition (IAD).

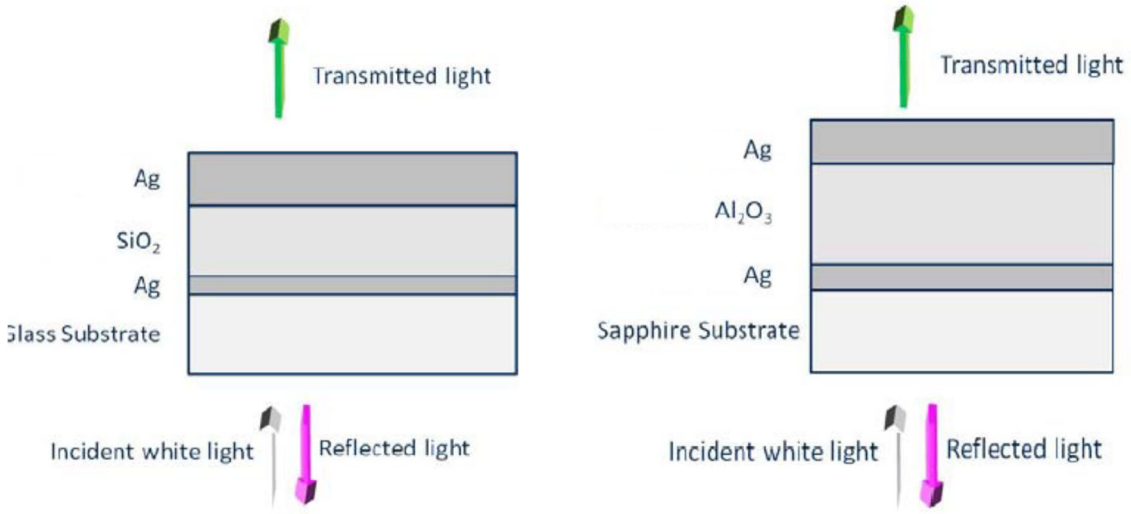

Figure 18. Optical Microcavity Structures: Ag-SiO_2 (left) and Ag-Al_2O_3 (right).

For both structures, the devices have wider FWHMs and shallower minima than those predicted. It should be noted that some of the SiO_2 OMC structures were unstable, hence, these exhibit different reflectance spectra. The SiO_2 AOMC structures were also found to degrade even more over time and with light/atmosphere exposures due to poor adhesion between SiO_2 and Ag [8]. Under dynamic loading, the signal-to-noise ratios were very low and spectral responses relied heavily on significant data processing/filtering to distinguish and monitor spectral shifts, due to insufficient depths in characteristic minima exhibited for both fabricated SiO_2 and Al_2O_3 OMC structures which can hinder their utility as dynamic loading sensors. Therefore, different designs with increased sample stability, minima depth, and narrower FWHM were developed and further investigated.

For this investigation, the OMC structures were fabricated on commercially available glass or sapphire substrates. The substrates were thoroughly cleaned using organic solvents and acid (methanol & hydrochloric acid). Ag mirror layers were deposited, by electron-beam evaporation, which was chosen over sputtering to provide higher surface and interface smoothness. The cavity layers were deposited using ion-assisted deposition (IAD); selected for its capability for high spatial uniformity, simultaneous deposition of different dielectric layers, and particularly its accurate control over the deposition rate and application of plasma excitation for enhancing atomic mobility so as to achieve high density film depositions and sharp interfaces at low temperatures (20 °C). Note that achieving a high-density cavity layer is very important as density directly affects the refractive index and dynamic loading of the structure. Therefore, the use of IAD, which provides precise control over deposition rate is very important and is a less invasive deposition technique compared to sputtering techniques.

The thicknesses of the deposited layers were characterized using test coupons and a profilometer and the reflectance spectra and refractive indices were measured using a Filmetrics thin film interferometer system. After successful validation of the static spectral behavior, the fabricated AOMC structures were mounted in the laser shock compression package for the dynamic loading experiments.

Figure 19 shows the time-resolved spectral response of an Ag-SiO_2 OMC structure under a laser-driven shock load of ~6.8 GPa. The time-resolved blueshift (calculated using the method of moments proposed by Brown et al. [9]) shows excellent, sub-nanosecond temporal alignment to the velocity profile of the silver mirror layers measured via PDV, matching the rise, peak, and shoulder at *t=44 ns* very closely. The maximum observed blueshift of 46 nm (using empirical models of SiO_2 compression and refractive index change developed by Setchell [10]) matches the theoretically predicted value of 48.5 nm to within ~5%, indicating that the previous discussion of blueshift mechanisms in OMCs [7] is potentially a good description of the response of the structures to dynamic loading. Further studies that will explore the response of the AOMC structures to a wide range of pressures is underway to further validate these predictive models.

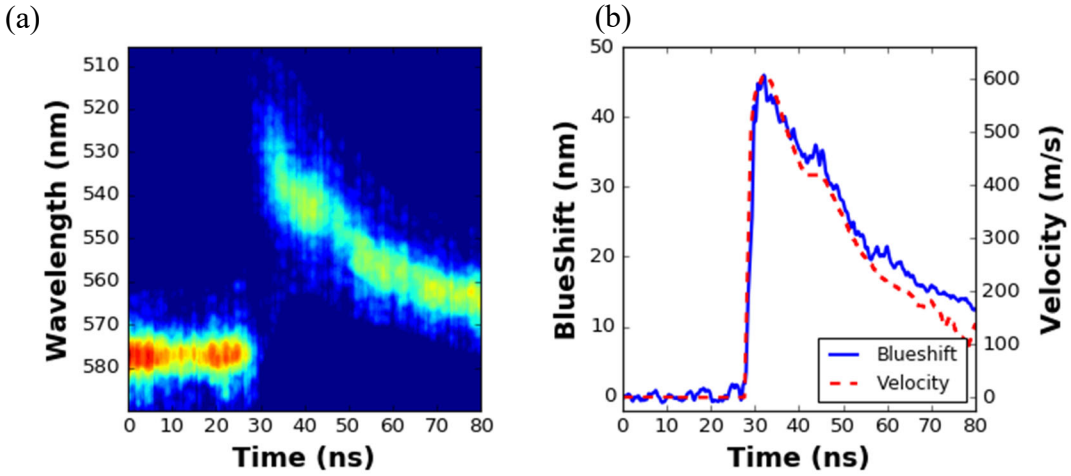

Figure 19. (a) and (b) The corresponding blueshift of the reflectance peak (blue solid curve) and the velocity profile from the PDV measurement (red dashed curve).

Figure 20 shows the time-resolved spectral response of an Ag-Al_2O_3 OMC structure under a laser-driven shock load of ~8.6 GPa. The time-resolved blueshift (calculated using the method of moments proposed by Brown et al. [9]) shows good temporal alignment to the velocity profile of the silver mirror layers measured via PDV (within ~2 ns), though not as well matched as the Ag-SiO_2 OMC data. However, the signal-to-noise ratio of this experiments was relatively poor, so the error on the blueshift magnitude and temporal position may have moderate error. Future experiments with higher-quality data will better illustrate the true temporal response of the Ag-Al_2O_3 OMC structures. Also, note that the magnitude of the pressure shift is significantly lower than that observed for the Ag-SiO_2 OMC, due to the significantly higher modulus of Al_2O_3.

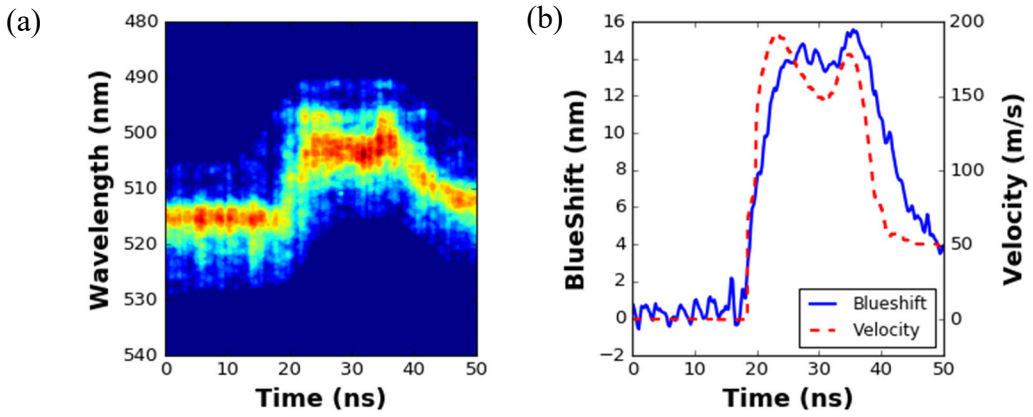

Figure 20. (a) Time resolved reflectance spectrum of an Ag-Al_2O_3 OMC structure taken by the streak camera successfully capturing the shift in reflectance peak caused by an applied shock pressure of ~8.6 GPa and (b) the corresponding blueshift of the reflectance peak (blue solid curve) and the velocity profile from the PDV measurement (red dashed curve).

Finally, Fig. 21 shows the time-resolved spectral response of an Ag-PMMA OMC structure under a laser-driven shock load of ~2.0 GPa. The time-resolved blueshift (calculated by tracking the peak of a spline fit) shows qualitative temporal fit to the expected laser-drive shock profile, though notably expanded in time due to the viscous nature of the PMMA cavity's response to the shock load (similar to what was observed with the quantum dots in the PVA polymer matrix). The signal-to-noise ratio of both the samples and experiments was quite poor, and more work is needed to address challenges in the fabrication of these structures. Future experiments with higher-quality data will better illustrate the true response of the Ag-PMMA OMC structures. Also, note that the magnitude of the pressure shift is relatively high for the low pressure of ~ 2 GPa, due to the significantly lower strength of the PMMA cavity.

Spatially Resolved Dynamic Sensing with Multilayer Structures

A major goal of the present work is the development of time-resolved sensing devices that can provide information of the complex material states observed in particulate and reactive materials. Often this behavior is characterized by a temporally and spatially varying pressure load, which many current experimental diagnostics struggle to accurately capture. To investigate the response of the OMC multilayer structures to temporal and spatially varying dynamic load, a simplified step-load

experimental setup was developed, as shown in Fig. 22. The qualitative response of a similar structure was also simulated in COMSOL Multiphysics simulation, utilizing the optical FEM method. The peak pressure state was simulated, consisting of a high and zero pressure with a small transition region between the two. The schematic and dimensions of simulation are shown in Fig. 23, along with initial and peak pressure spectra. The key feature in simulated peak pressure spectra is the presence of two distinct cavity modes, corresponding to high and zero pressure regions of the SiO_2 AOMC. This simulation provides a clear indication of the type of spectrum that should be observed in the experiment described in Fig. 22.

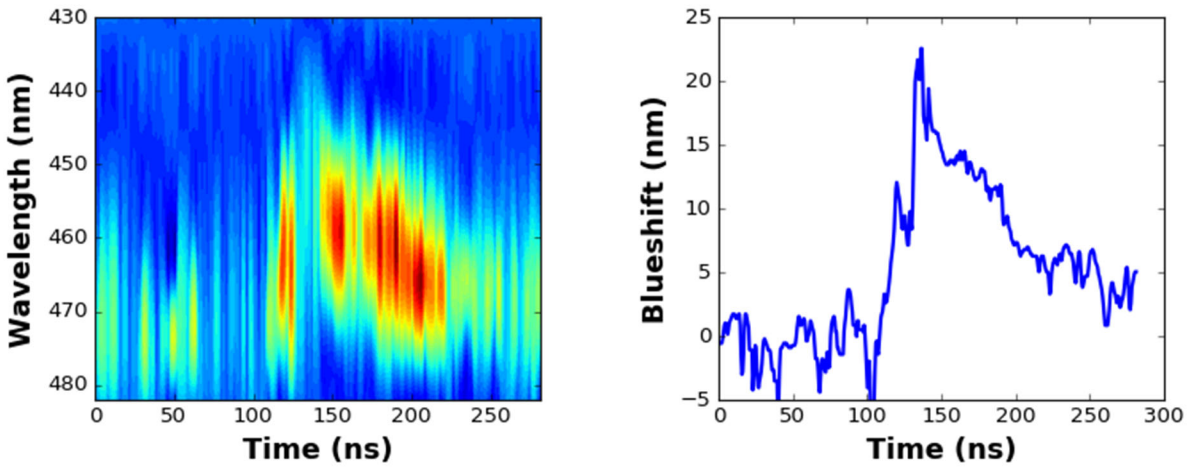

Figure 21. (a) Time resolved reflectance spectrum of Ag-PMMA OMC structure taken by streak camera successfully capturing shift in reflectance peak caused by an applied shock pressure of ~2 GPa and (b) corresponding blueshift of reflectance peak. Note that the time-scale of the pressure induced blueshift is increased due to the viscous nature of the response of the PMMA cavity.

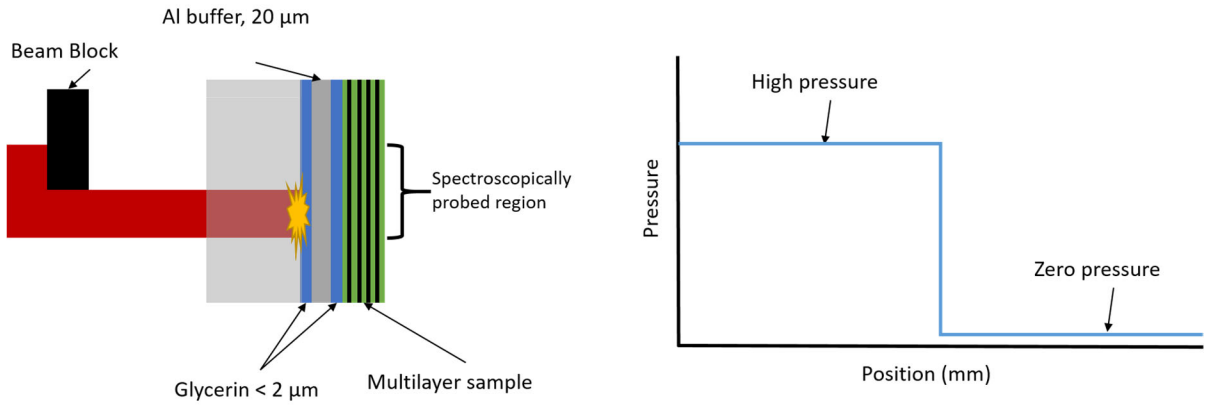

Figure 22. Schematic of laser-driven shock setup designed to induce temporally and spatially varying pressure in multilayer sample. Use of a beam block (left) creates step in pressure (right), which both regions captured in spectrograph/streak camera data collection setup. Temporal shape of pressure will be same as in previously described experiments, shown in Fig. 26.

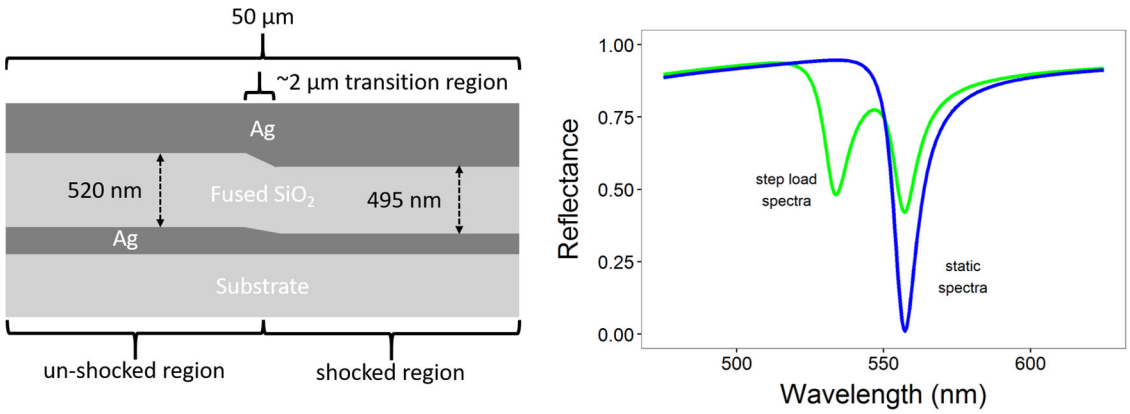

Figure 23. Schematic of COMSOL multiphysics simulation predicting the spectral response of SiO_2 AOMC structure, subjected to heterogeneous stepped pressure. Initial (blue) and peak pressure spectra (green) are shown on right. The peak pressure spectrum shows two distinct cavity modes, corresponding to shock and un-shocked regions. The spectroscopically probed area contains both regions, each contributing approximately 50% of the total optical power.

Figure 24 shows the experimental results of step load experiment (ΔP = ~3.5 GPa), along with individual spectra corresponding to initial, peak pressure, and released states in multilayer. The presence of two distinct cavity modes is clear, with spectral and temporal profiles qualitatively matching the expected spectral and temporal history of the zero and high pressure.

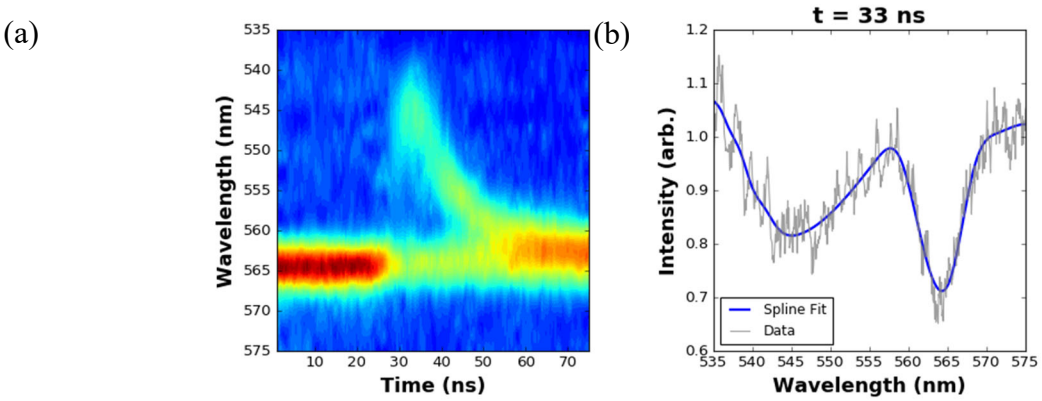

Figure 24. (a) Spectral and temporal response of SiO2 AOMC device to a stepped pressure load of 0 and ~3.5 GPa. A multi-mode spectral response is clearly observed, with both the 0 and ~3.5 GPa regions showing unique spectral and temporal profiles corresponding to the expected profile of the laser-driven shock pulse. (b) Individual spectra corresponding to t = 33 ns (the peak pressure state), showing the clear separation of the separate peaks.

Figure 25 shows a similar experiment, but at lower pressure difference between the step (ΔP = ~2 GPa). This demonstrates the ability to resolve the different spectral peak positions despite a relatively small difference in pressure.

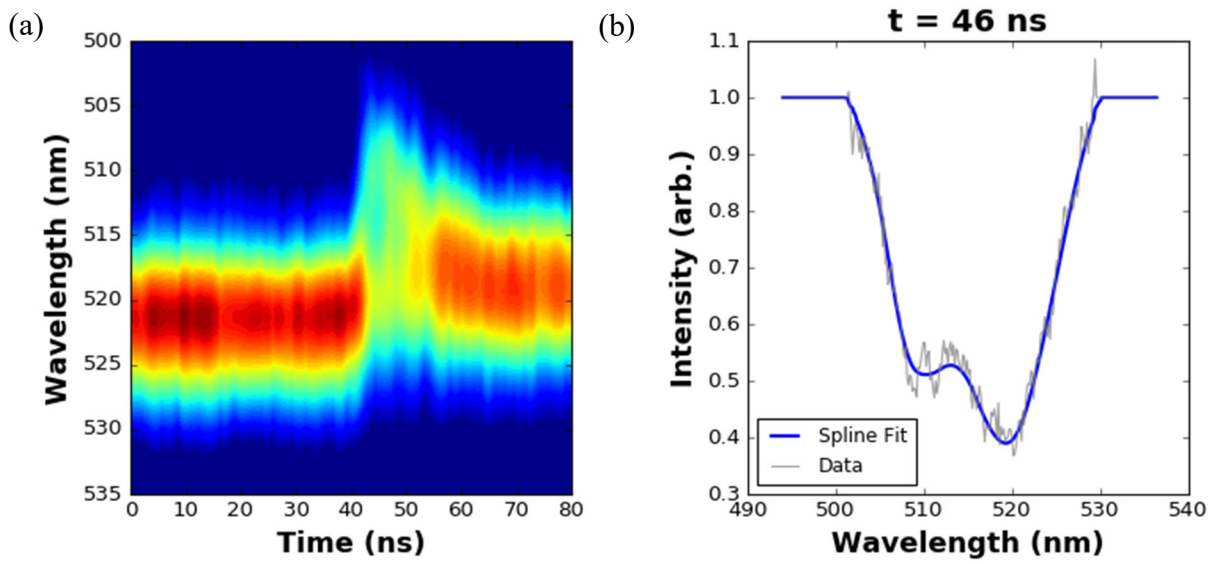

Figure 25. (a) Spectral and temporal response of SiO2 AOMC device to a stepped pressure load of 0 and ~2.0 GPa. A multi-mode spectral response is clearly observed, with both the 0 and ~2.0 GPa regions showing unique spectral and temporal profiles corresponding to the expected profile of the laser-driven shock pulse. (b) Individual spectra corresponding to t = 46 ns (the peak pressure state), showing the combined zero and ~2.0 GPa pressure spectral profiles, with lower, but still sufficient separation to resolve the individual peaks.

Additionally, for a more complete analysis of the spectral data from a heterogenous dynamic load, a novel analysis approach based on an extension of the moment analysis by Brown et al. [9] leverages the 2nd, 3rd, and 4th moments of the spectra (full-width-half-max, skew, and kurtosis, respectively) to more fully describe the temporal evaluation of the spectral profiles. This method should extract even more information from the time-resolved spectra that can be correlated to features of the dynamic load.

Finally, an important feature of the any spatially resolved sensing method is the spatial resolution. Experiments to explore the practical resolution of the multilayer structures are currently underway, but a theoretical analysis is also important to identify the fundamental limits of the devices. By extending the COMSOL analysis described previously, the separation between the stepped pressure load and width of the probed region was slowly decreased until the individual peaks could no longer be discerned from the spectra. This establishes the theoretical maximum spatial sensitivity of the OMC structure, defined as the ability to resolve to uniform, but different pressure regions separated by some transition region. Figure 26 shows a plot of the spectral response as the transition region decreases. Note that this analysis does not consider more practical concerns such as illumination and collection of the reflected light from the OMC, which in practice are likely to be the primary limiting factors affecting spatial sensing resolution. Nevertheless, the maximum spatial sensitivity of the structures is high, indicating that spatial separations in pressure of < 1 um could be theoretically be resolved by the OMC structures.

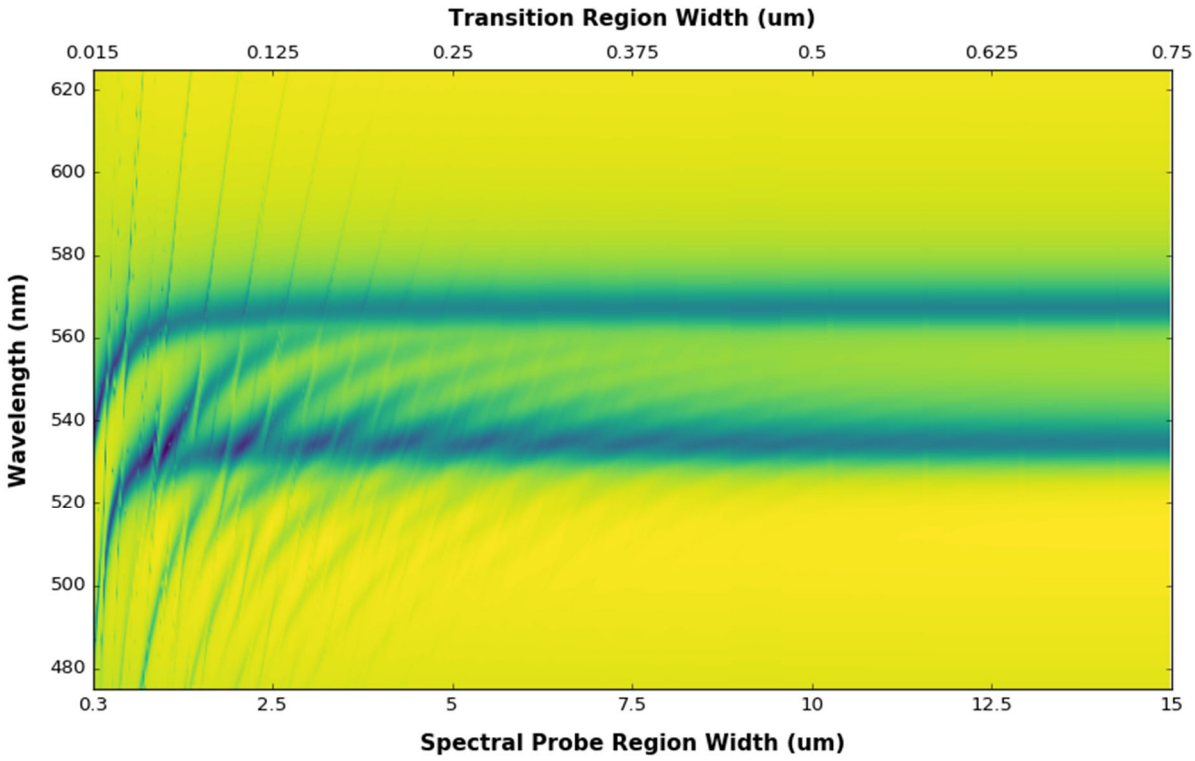

Figure 26. Contour plot showing the spectral profile (vertical and out-of-page axes) as a function of decreasing spectral probe width and transition width between a stepped pressure load. The individual peaks (corresponding to the individual pressures) are clearly visible at the right hand side of the image, with decreasing clarity and quality of the spectra as the separation between the stepped pressure loads decreases toward the left.

In order to check the utility of the OMC optomechanical sensors to testing pressure distributions in a truly heterogeneous system, we considered a composite sample with spherical particles in an estane polymer matrix. Coupling FEM mechanical and optical simulations we predicted the strain and pressure variations associated with the shock compression of the composite and subsequent effect on the response of the OMC mounted on the back surface of the composite. Figure 27 shows a schematic of the set-up and the simulated variations in localized strain and pressure below and between particles and below estane matrix, upon shock compression of the composite at 6 GPa. The corresponding streak pattern and spectral profiles at three different time scales, are shown in Figure 28. Intensity ratios for each peak can be used to obtain an estimate of the area fraction of the sensor witnessing different pressures.

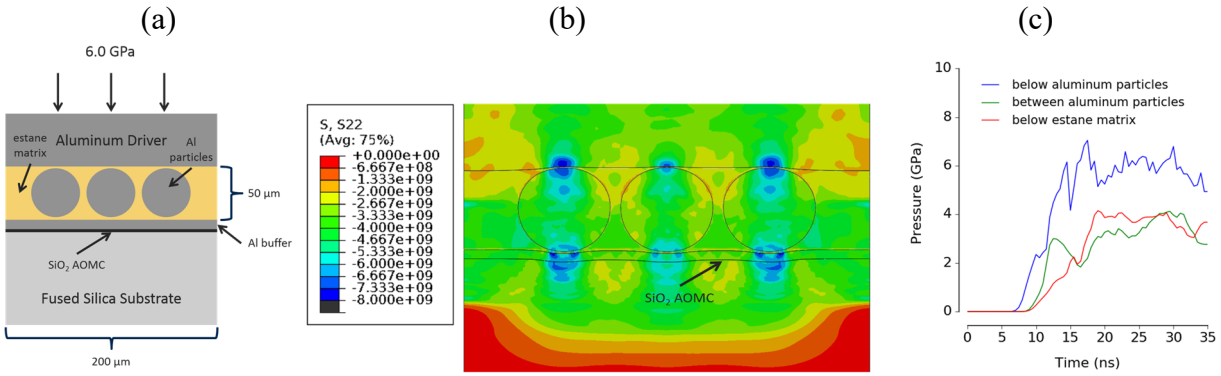

Figure 27. Schematic of (a) set up of composite with three spherical particles in estane matrix subjected to laser driven shock propagated through Al driver at 6 GPa and (b) FEM simulations of strain and pressure below and between particles and below estane matrix.

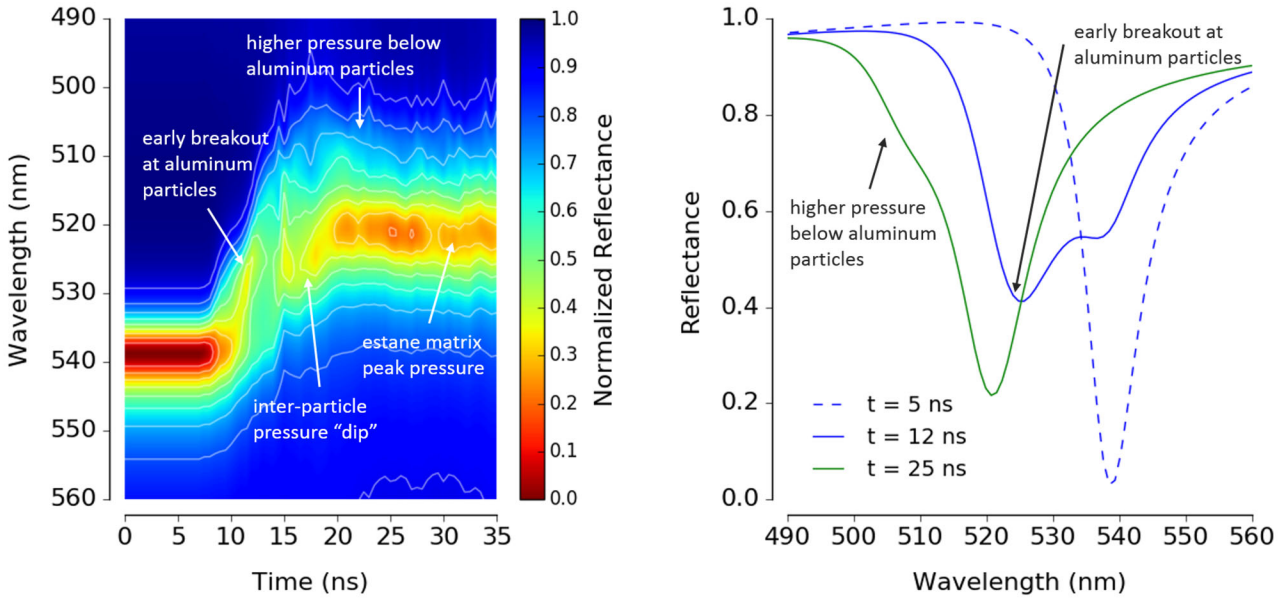

Figure 28. Simulated (a) streak pattern showing wavelength shifts from shock compression of particles and estane matrix; and (b) spectral profiles at three different time scales showing breakouts in blueshifts associated with pressure variations due to differences in elastic and plastic properties.

Based on the understanding obtained from the simulations, laser shock compression experiments were then performed with the OMC placed as a backer sensor sandwiched between the composite sample (200 µm Silica particles embedded in epoxy) and PMMA backer, as shown in the schematic illustrated in Figure 29 (a). The corresponding streak image of the spectral profile indicating change in emission (blueshift and intensity change), is shown in Figure 29 (b).

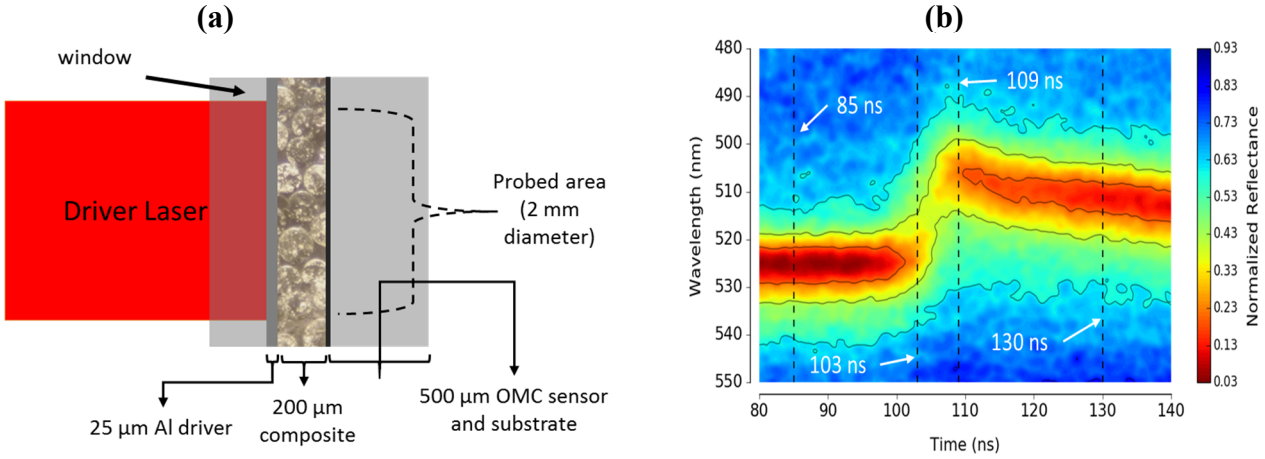

Figure 29. (a) Schematic of laser shock compression experiment set-up with OMC structure placed as backer gauge sandwiched between a composite sample (200 µm Silica particles embedded in epoxy) and PMMA backer, and (b) corresponding streak image of spectral profile indicating change in emission (blueshift and intensity change).

The time-resolved blueshift change time-synchronized with the PDV particle velocity profile shown in Figure 30, reveals the clear correlation of stress (pressure) evolution as a function of time with the corresponding change in velocity versus time captured with the PDV.

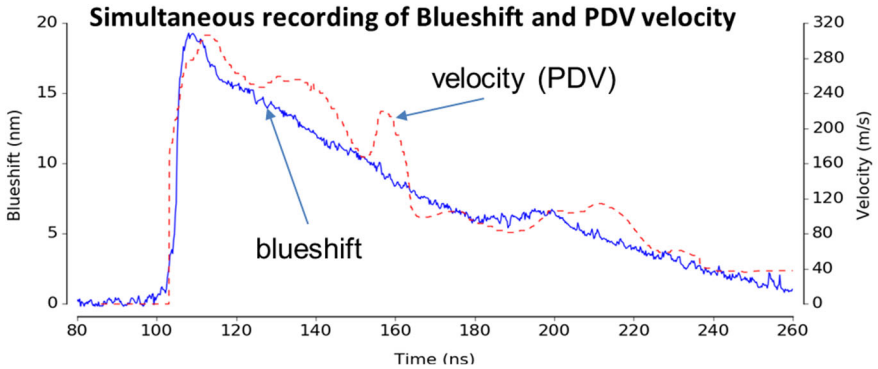

Figure 30. Time-resolved blueshift change time-synchronized with PDV particle velocity profile

The break-outs seen in the streak image in Figure 29(b) are characteristic of the pressure distributions arising from the presence of heterogeneities (particles in matrix). Correspondingly, the distributions in pressure were correlated, to generate a mapping of the area fraction of the planar surface of the composite sample subjected to different shock-induced pressures based on blueshifts monitored by the OMC. The time-resolved variations in such pressure distributions are plotted in Figure 31.

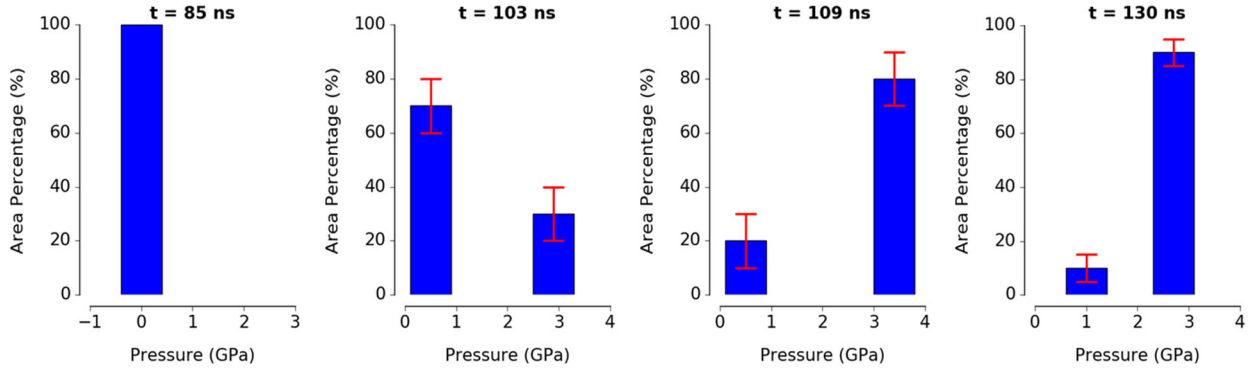

Figure 31. Time-resolved variations in pressure distributions showing mapping of area fraction of planar surface of the composite sample subjected to different shock-induced pressures.

Future experiments will involve wavelength-modulation to generate an two-dimensional pressure mapping of regions subjected to actual pressures, which can be capture using a framing camera.

Summary and Conclusions

The work performed during the past year on the use of OMC sensor has involved simulations and experiments to investigate their potential for dynamic sensing of laser-shock generated pressures. The results indicate that the OMC structures present an inherent ability to distinguish spatially resolved states. With a suitably high signal-to-noise ratio and appropriate spectral sensitivity, many different spectral-temporal paths from dynamic loading of complex heterogeneous material correlating well with specific time-resolved pressure history of the entire probed area in the sample. Future work is geared towards scaling up the use of commercially-acquired OMC sensors with use on experiments performed with gas gun experiments.

3. Thermoreflectance-based technique for full-field temperature measurements in dynamic experiments (Imperial College London)

3.1. Overview

The research conducted at Imperial College London was directed towards spatially- and temporally-resolved measurements of non-uniform thermal landscapes in Heterogeneous Reactive Materials (HEMs) under dynamic loading conditions. This project complements the GT pyrometry-based effort by exploring the alternative technique of dynamic reflectance thermometry (DRT). The key intended outcome of this effort was the DRT diagnostic for simultaneous temperature and deformation field measurements and demonstration of the capability of this technique to capture rapid local changes in temperature (hot spots) in HEMs during high-rate loading. One of the main advantages of the DRT technique is that it can be used with “standard” visible-based high-speed cameras, notwithstanding intrinsic differences in frame-rate and resolution, to simultaneously visualize the evolving temperature and deformation fields. The key characteristics of the diagnostic are:

(1) uses a gold film as a sensor/gauge on the investigated specimen,

(2) provides measurements of temperature and deformation fields with high spatial (submicron) and temporal (microseconds and shorter) resolutions,
(3) is robust against non-temperature-related changes (e.g., sample tilt, surface roughness),
(4) utilises a stable illumination source free from uncorrelated spatial/temporal artefacts,
(5) is relatively portable, allowing straightforward integration on various dynamic loading platforms, e.g. drop-weight, SHPB system, gas gun, etc.

The following sections summarize the results of this 3-year programme, and suggests directions for future work.

3.2. Dynamic Reflectance Thermometry

The basic concept of thermoreflectance is that any change in a material's temperature has an influence on its optical and electrical properties. The measurement of the change in reflectance is made on the surface of the material with respect to time, and the collected data are matched to a model with coefficients that correspond to its thermal properties. The model, however, must be calibrated using experimental data for the same material. It is also important to note that the effect of temperature on the optical properties of most materials is relatively small and therefore challenging to capture at high strain-rates. This is because the acquisition of high-speed diagnostics is often noise limited, and the relative change in the reflected signals is often below the noise floor of the diagnostic used in these measurements. Only for certain metals, such as gold, do the changes in reflected signals become perceptible with respect to their optical properties, temperature, and specific illumination wavelength [1,2].

3.2.1. Reflectivity of Gold

As many materials of interest exhibit extremely low changes in reflectance with temperature, a gold sensor may be used (sputter-deposited gold films onto the specimen surface) to compensate for this weak dependence. Given their thermal transport properties, coupled with similar optical properties for bulk and thin films, gold films having a thickness less than 300 nm can assure fast equilibrium (within tens of nanoseconds) and sub-microsecond temperature measurements of the material of interest. One of the requirements of this technique is that the gold sensor must be characterized as prepared since the optical constants of gold can vary with specimen preparation, porosity, grain size, or changes in the microstructure through heating [2]. The concept of thermoreflectance measurements and variation of the reflected signals from a gold surface with respect to temperature and illumination wavelength are shown in Fig. 32. The figure also shows the reflectance normalized to room temperature as a function of the illuminating wavelength [Fig. 32(c)]. Note that the reflectance ratio inverts on either side of a 500 nm crossing point; the ratio significantly increases at wavelengths ~480 nm and decreases at wavelengths ~532 nm. The figure also shows the reflectance change of the two characteristic peaks [indicated by the arrows in Fig. 32(c)] with respect to temperature [Fig. 32(d)].

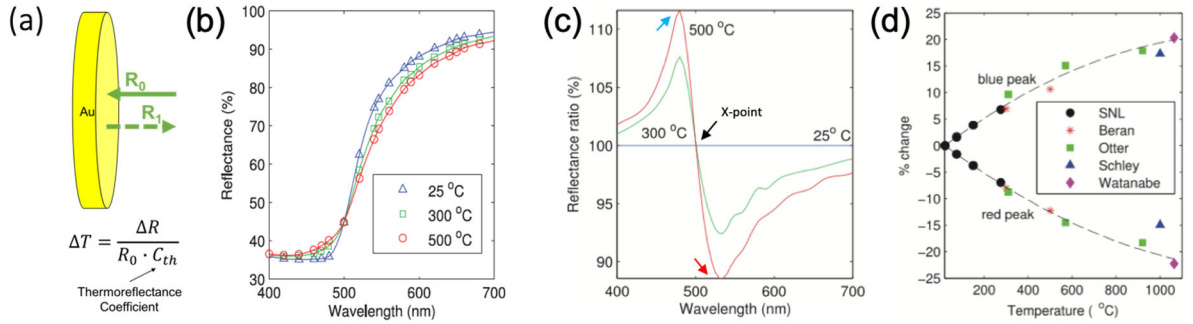

Figure 32. (a) concept of thermoreflectance measurements;(b) gold reflectance at different temperature in the spectrum of visible light; (c) reflectance ratio spectra for gold (normalize to room temperature values); (d) reflectance changes of the two characteristic peaks (shown in subfigure c) with respect to temperature [11].

3.3. Concept of an Experimental Platform

With the above principles in-mind, a general approach for conducting dynamic temperature measurements through reflectance measurements was conceived, and is shown in Fig. 33. The optical system would take as its input light from a specifically chosen illumination source(s). This light would be diverted to a target of interest, on the surface of which a thin layer of gold would be deposited. The reflected light from this surface would be collected by an objective lens which, after being split into separate spectral channels, would be imaged at an output prism. This split image would subsequently be imaged by a high-speed camera, allowing the reflected light from two specific wavelength bands to be monitored throughout an experiment.

This preliminary design left several questions to be addressed:

1. What types of suitable light sources are available and what are their limitations?
2. What wavelength ranges should be used for the different imaging channels?
3. Can digital image correlation be performed with a gold film?

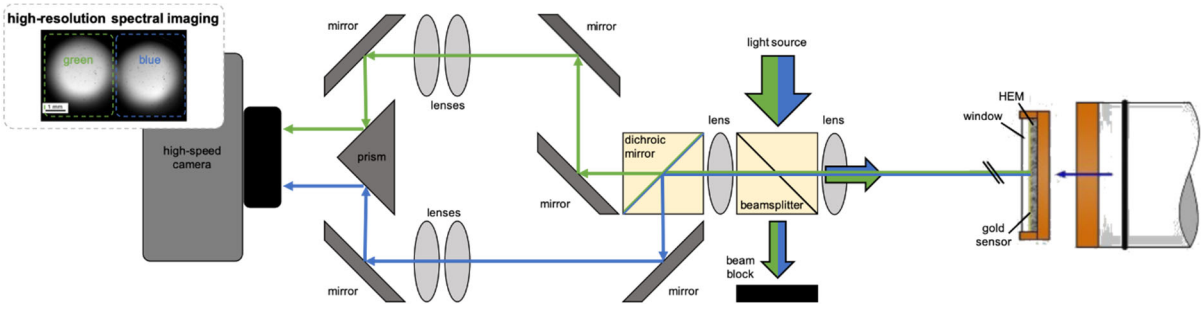

Figure 33. Concept of an experimental platform for the measurement of dynamic temperature fields in a plate-impact experiment. The system shown illuminates a specimen with discrete wavelengths, which are subsequently separated and imaged onto adjacent halves of a single high-speed camera. The choice of illumination wavelengths is chosen on the basis of the optical properties of the specimen or sensor material.

3.4. Light Source Evaluation

High-speed DRT measurements require significantly intense light to provide images with high contrast and signal-to-noise ratios during the necessarily short exposure times. Thus, a good light source should not only have high-brightness with spectral emission in the wavelength range of interest, but also high levels of stability and repeatability of output intensity. These factors are essential for reflectance measurements that require sequential data acquisitions with sampling rates up to few MHz. Although there are many high-power light source technologies available on the market, we found that their potential use in such measurements is limited. The research highlights from these trials are listed below:

1. Xenon-based flash lamp
   Flash lamps can provide a reasonable amount of light across the visible spectrum for capturing the dynamics in high-speed events. Unfortunately, these light sources suffer from temporal variations in the power output, which was not suitable for the thermoreflectance method. Additionally, the amount of light at discrete wavelength of interest (e.g.: two characteristic peaks at 532 nm and 480 nm indicated by the arrows in Fig. 32(c)) was also limited. The spectrum of a typical flash lamp is show in Fig. 34.

2. White LED emitter (LZP-00NW0R)
   This light source could dissipate up to 90W of power on a compact 12 mm×12 mm footprint, and provided a reasonable amount of white light for high speed photography. Also, it could be assembled into compact, closely-packed arrays. For example, an array composed of 8 LEDs was sufficiently intense to enable low-jitter, high-speed imaging of dynamic compression experiments with exposure times of 5 μs and longer, enabling measurements of surface strains with the DIC technique. However, the amount of filtered light at the wavelengths of interest [e.g.: two characteristic peaks at 532 nm and 480 nm indicated by the arrows in Fig. 32(c)] was insufficient for full-field dynamic temperature measurements at the same exposure times.

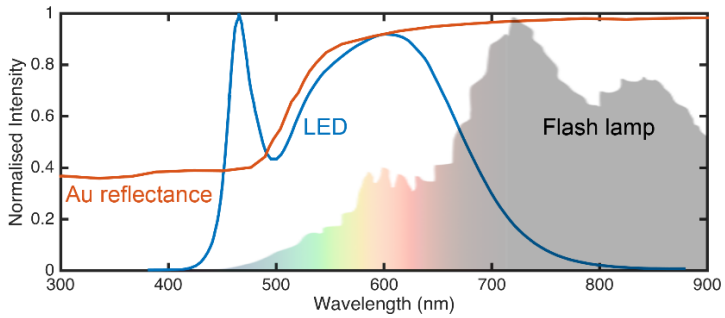

Figure 34. Normalised emission spectrum as a function of the wavelength for the flash lamp and a white LED emitter (LZP-00NW0R). The figure also shows the reflectance of gold in the visible light spectrum. The flash lamp lacks sufficient emission around the 500 nm crossing point of the Au reflectance spectrum.

3. Laser-based illumination
   Lasers can provide high energy and long-term output power stability at discrete wavelengths. These light sources also have highly directional output, ease of propagation and focusing using standard optics, and thus high corresponding intensity at the measurement site. However, lasers introduce additional challenges, as their coherence

results in undesirable spatial modulations in intensity (speckle) at the image plane. Efforts to eliminate or minimise the speckle effect were explored using the following approaches:

(i) wavelength diversity by combining the output from slightly detuned lasers,
(ii) polarization diversity by using light with different polarization from several slightly detuned lasers,
(iii) angle diversity by illuminating the specimen under different incident angles of light,
(iv) reduction in spatial coherence through the use of diffusers (static and moving),
(v) fibre-based coupling and mixing of the output light from several lasers,
(vi) optical path length modulation (vibrating fibres) while running tests,
(vii) combination of two or more methods above mentioned.

The obtained results have not been completely satisfactory. For example, Fig. 35 shows a calibration target (Negative USAF1951) illuminated with a static laser beam (fibre-coupled) and an engineered laser beam (coupled into vibrating fibre and diffused). It is clear that the quality of the image obtained with a static beam is unacceptable for our application. Note a high speckle contrast of 0.44 (defined as the ratio of the standard deviation of the intensity to the average intensity). The image obtained with an engineered beam has very low speckle contrast (0.02). However, the exposure time has to be long enough (50 ms in this case) in order to obtain a sufficient level of beam homogenization. This time scale is several orders of magnitude longer than is required for our applications. To this end, we were not able to fully eliminate the spatially coherent nature of the laser beam (i.e., subjective speckle noise) over the time domain required for this project (< 1 μs). However, this work helped to define the output power required to achieve microsecond (or less) exposure times at magnifications sufficient to resolve micrometer-scale features. Based on this work, it was also decided to direct attention towards single-colour LED emitters, which have broader spectral width and consequently lower coherence (the speckle contrast compared to diode lasers is negligible). Although these light sources have much lower output power when compared to white-light LEDs, their output is highly collimated, leading to higher potential intensities at the measurement surface.

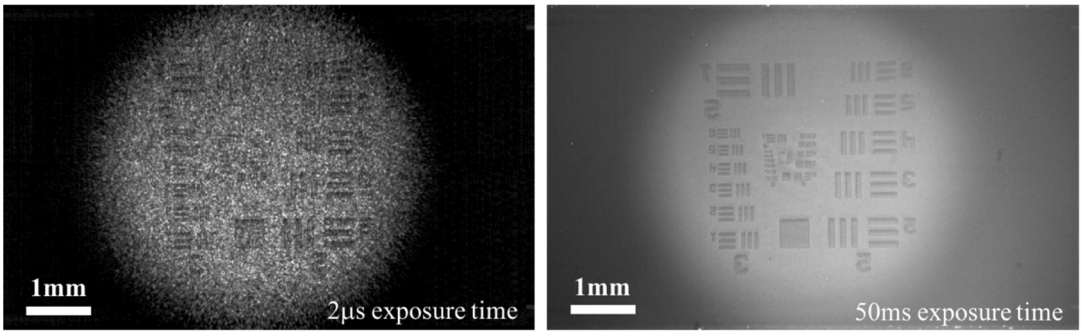

Figure 35. Illumination of the calibration target (Negative USAF1951) using: (left) static laser illumination and high-speed camera with 2μs exposure time, and (right) engineered laser illumination and high-speed camera with 50ms exposure time. The speckle contrast is 0.44 and 0.2, respectively.

4. EQ-99X LDLS™ broadband laser-driven light source.
   This light source provided a good amount of white light for high-speed imaging. However, an undesirable "flickering" issue (varying light intensity in time) was reported during the tests, as presented in Fig. 36. This was caused by the modulation of the laser introduced to lower the overall noise of the LDLS (the DC laser drive current was modulated at a rate of about 50kHz). The "flickering" introduces an unacceptable error in the thermoreflectance measurements; a peak-to-peak uncertainty of 8% in reflectivity corresponds to ~350 degrees C. The amount of light at discrete wavelengths of interest (i.e.: 532 nm and 480 nm) is also limited.

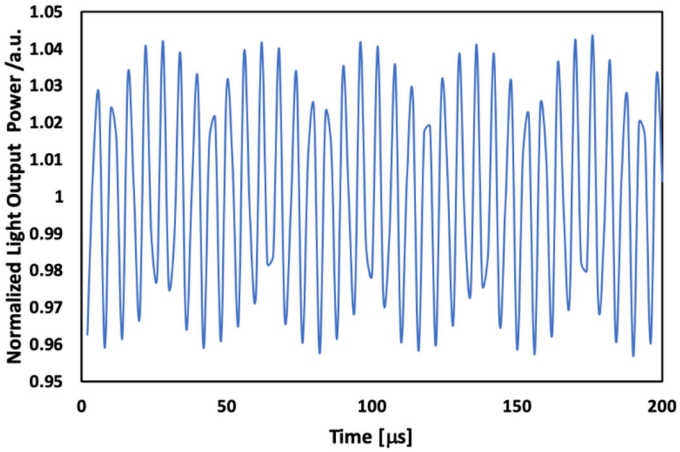

Figure 36. Normalized light output power with respect to time of the EQ-99X LDLS™ light source. The intensity was observed to fluctuate at ~175 kHz, which would lead to uncertainties in temperature of up to 350 degrees C.

5. Prizmatix UHP-T-LED-405 and UHP-T-LED-520
   These LEDs produce narrow spectral emission bands of *blue* and *green* light and provide the best compromise solution for spatial and temporal measurements of reflectance with discrete wavelengths bands. Using the LED modules, a high-brightness, stable, and speckle-free illumination was obtained that allowed speckle-free imaging of objects with microsecond acquisition. Figure 37 shows the light source and normalised emission spectrum as a function of the wavelength for the individual LEDs. It should be noted that one important characteristic of the LED technology is that the spectrum can shift by changing the LED drive current. Here, both LEDs driven at maximum current density shift the central wavelength of the emission spectrum away from the low current peak. In case of the *green* LED (Prizmatix UHP-T-LED-520), the central wavelength of the LED shifts from 532 nm to 523 nm by adjusting current between the threshold and maximum levels. The spectral width of the source (Full-Width-at-Half-Maximum) is approximately 36 nm, and the collimated optical power output is up to 1.2W. The central wavelength of the emitted light from the *blue* LED (Prizmatix UHP-T-LED-405) can shift from 406 nm to 402 nm by varying the drive current from the threshold to maximum value. The spectral width of this light source (Full-Width-at-Half-Maximum) is approximately 19 nm, and the collimated optical power output is up to 3.8W. The changes in emission spectral shape can be, however, ignored since narrow bandpass filters are used in the experimental platform that limit the bandwidth of the output signal to the band allocated for thermoreflectance

measurements (also shown in the figure). Thus, in such configuration, the errors in measurement might occur in two scenarios: (i) when the LEDs are driven at different illumination intensity levels prior to (when exploring the temperature dependent optical properties of gold on the test specimens) and during the tests and (ii) when voltage or current fluctuations are present in the circuit to which the LEDs are connected. Both are minimised by a high-stability power source with precise adjustment range of target parameters.

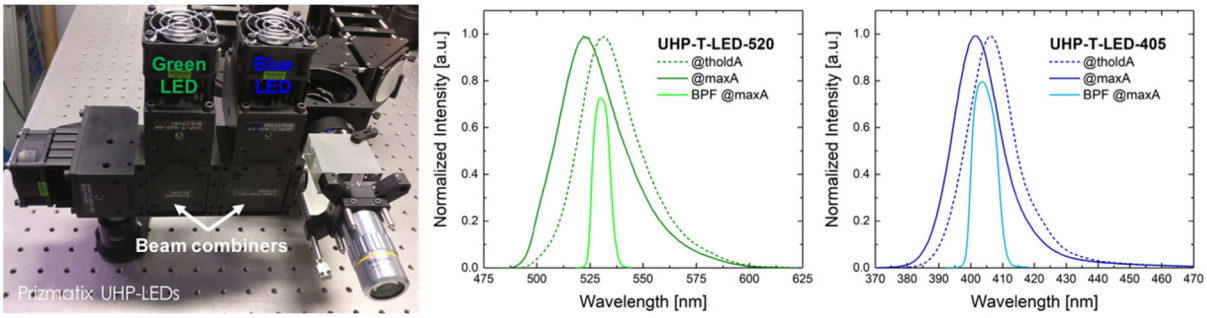

Figure 37. Multi-LED light source and normalised emission spectrum as a function of the wavelength for the individual LEDs. The spectrum can be seen to shift to lower wavelengths with driving current. A bandpass filter was used to narrow the spectrum for each wavelength band.

A quantitative analysis of intensity fluctuations in emitted light from stabilised (powered-up for > 1 min.) LEDs was performed by evaluating the intensity of light incident on the photodiode (Thorlabs DET10A/M). Figure 38 shows the power spectrum results, which are based on the output voltage signals acquired by the detector for 1 s at a sampling rate of 200 kHz. Note that none of the voltage signals (1 ms long signal sequences are shown in the insets of subfigures) are contaminated with drift or visually evident periodic components. As a matter of fact, the potential voltage fluctuations caused by the emitted light from the LEDs are within the range of the background noise level in an electronic system (combined vertical noise of the oscilloscope and the photodiode) and have comparable RMS amplitudes of voltage fluctuations. Thus, it is expected to see the power spectrums of nearly constant and equally spread values over all frequencies. This, in turn, suggests a stable and constant light emission from the LEDs over a wide range of temporal scales.

Figure 39 shows the experimental reflectance ratio spectra for gold and the projected emission wavelengths of the two LEDs used in this study. For reference, see the normalised emission spectrum as a function of the wavelength presented in Fig. 37. As discussed in *Section 3.2.1.*, the reflectance changes occur on either side of 500 nm, with the ratio spectrum significantly increasing in the ~480 nm peak and decreasing in the ~532 nm peak. The DRT measurements are made with narrow bands of wavelength at 405±10nm and 532±10nm, respectively. These are indicated in the figure as *the wavelengths of interest*. In this configuration, the reflectance measurements with the *blue* light are essentially temperature insensitive (less than 1% change up to 500ºC), and with the *green* light changes associated with increases in temperature are much more evident (12% of change between the initial room temperature and 500ºC).

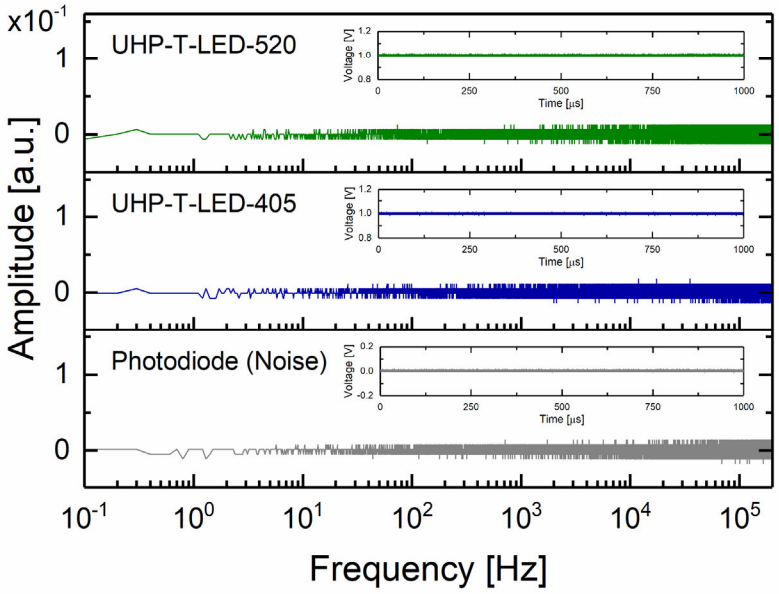

Figure 38. Power spectrum of intensity fluctuations for the individual LEDs and the photodiode (background noise). The insets show the original time-domain measurements, which reveal a stable intensity over a period of 1 s. The lack of distinct frequency components in the voltage signal implies a stable output over this extended measurement window.

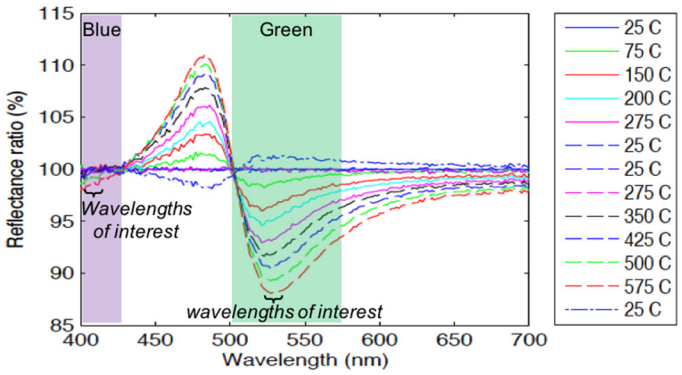

Figure 39. Reflectance ratio spectra for gold [12] and the projected emission wavelengths of the LEDs used in this study. A blue LED centred at ~405 nm was chosen to monitor non-temperature related changes in reflectance.

3.5 DIC-DRT Diagnostic

Over the course of the project several systems were constructed, which tested various challenges, such as: illumination, wavelength selection, combining DIC/DRT, optical component performance, and convenience (setup and alignment). The following subsections describe the primary designs to come out of this work.

3.5.1. Prototype of 3D DIC-DRT Diagnostic

Figure 40 shows a prototype of a combined 3D DIC and DRT diagnostic. In this configuration, the

surface of the specimen was illuminated with white light LED sources incident upon the target surface at a small angle with respect to the surface normal. The light reflected from the surface of the specimen was collected by separate objective lenses for the DIC and DRT channels, and image relayed to the high-speed camera as four independent optical channels. Two optical channels (seen in a top view of the diagnostic in Fig. 40) were used to collect and filter (using a bandpass filter at 480±20 nm and 532±20 nm) the light to provide two separate spectral bands for the thermoreflectance measurements. The principles of these temperature measurements are given in Section 3.5.2. (the final DRT design). The remaining optical channels (seen in a side view of the diagnostic in Fig. 40) collected the light reflected from the specimen at a specific angle with respect to the surface normal such that a 3D-DIC analysis could be conducted on the acquired high-speed images.

This system served as a successful proof-of-principal, however suffered from several limitations:

1. Resolution – the fully-distinct DIC and DRT approach relied upon individual objective lenses (doublets) for the various arms. Imaging at magnifications higher than 2x would require using stronger lenses (e.g. microscope objectives), which were not compatible with this design.
2. Vignetting – the small (1″ diameter) optics relative to the path length between optics led to vignetting of the collected light, resulting in poor efficiency.
3. Alignment – the four separate measurement arms, incident upon a pyramid reflector introduced too many degrees of freedom, and therefore required frequent alignment and calibration.
4. 3D DIC complexity – the local strain fields to be measured were primarily confined to 2D, so we could simplify the design to help with Point 1 above.

Finally, despite utilising an array of 8 azimuthally distributed white light LEDs, the amount of reflected light in the two chosen wavelength bands was deemed insufficient. As discussed earlier, although the net power dissipated by the white light LEDs was high (>300 W), the fraction of light emitted in the wavelength bands of interest and collected by the optical components was inadequate for our high-speed application. This configuration was therefore modified to introduce a beam-splitter into the system (between the DRT diagnostic and the specimen), which could take the collimated output of a laser or fibre-bundle and direct it normally to the specimen surface. The use of a beam-splitter in this manner reduced the maximum efficiency of the collection optics to 25%. This was offset by the use of powerful lasers and directional illumination, highlighting the distinct advantage of this technique.

3.5.2. 2D DIC and DRT Diagnostic

This design addressed many of the limitations identified in the previous system, such as separate optical channels for the DRT and DIC measurements, observations at fixed magnification level, efficiency of the optics, and the collection of reflected light from the illuminated surface. A prototype of this updated DRT diagnostic is shown in Fig. 41. The main optical breadboard holds and positions a light source (discussed later in the text) and an array of optical components mounted in a cage system. The path that light rays travel from the light source to the camera is as follows. First, a mixed beam of light provided by two LEDs (*green* and *blue* colours) is directed to a pellicle beamsplitter. The half of the incident light that propagates through this beamsplitter is reflected towards the specimen and the other half is transmitted through it and then blocked. The reflected light passes through the centre of the microscope objective and focuses on the surface of the sample. The light is

then reflected off the specimen back through the objective, beamsplitter, lens and strikes a longpass dichroic mirror at a 45° angle of incidence. At this location, the light is separated into two single-colour light beams such that the *green* light beam propagates through the longpass dichroic mirror and the *blue* light beam is reflected from it. Consequently, the beams are directed by a series of broadband dielectric elliptical mirrors to a knife-edge right-angle prism mirror, where the two light beams meet again and propagate parallel to each other with a small offset. On the path between the longpass dichroic mirror and the prism mirror, the light beams pass through a bandpass filter and two plano-convex lenses. The bandpass filters transmit a range of wavelengths of interest and filter out the light on either side of that range, while the lenses are used to establish an image plane at the edge of the right-angle prism. The distance between the specimen and the prism mirror is the same for both colour channels. Thus, both channels reconstruct an image with the same magnification at the focal point. As a result, an image formed on the sensor of the camera is composed of two images showing the same object illuminated by light of wavelengths 405±10 nm (right side image) and 532±10 nm (left side image), respectively. The use of a 405 nm LED rather than 480 nm, as in previous systems, was to correct for non-thermal effects, as explained in section 3.4.

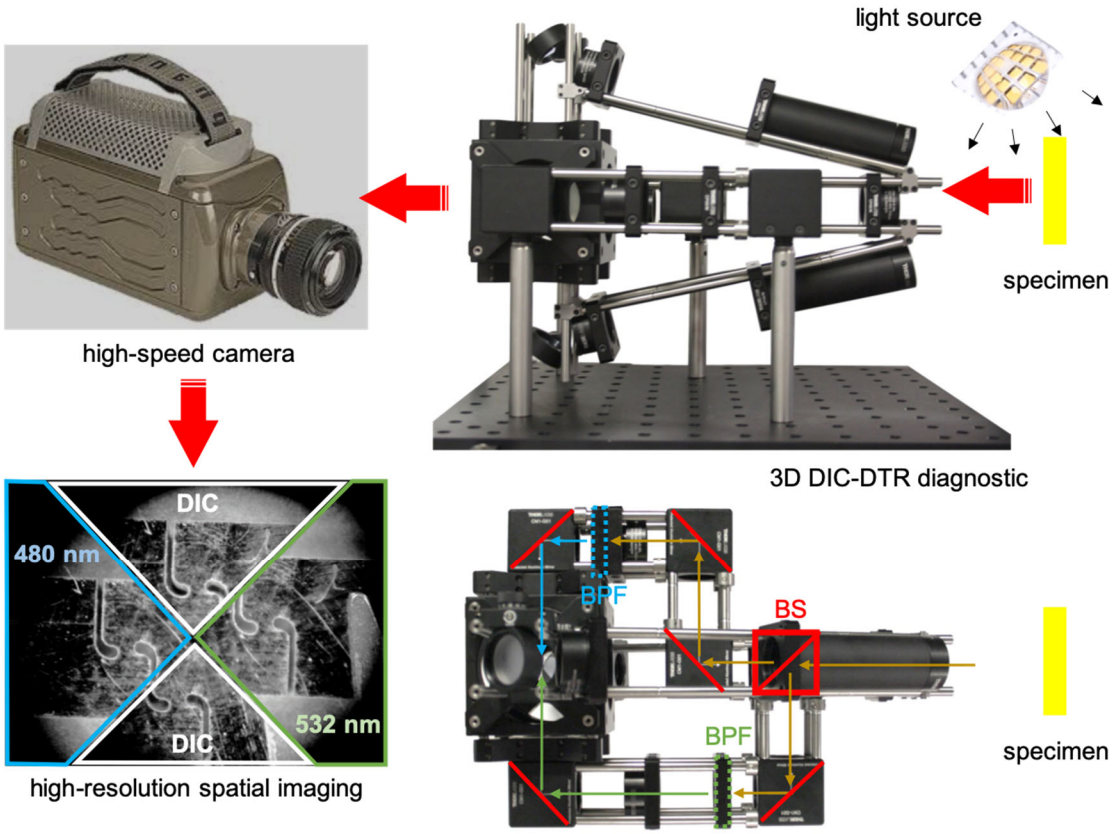

Figure 40. Experimental setup used with a high-speed camera for real-time measurements of temperature and deformation fields, where: BS – beam splitter, BPF – bandpass filter. The specimen is illuminated by an array of white-light LEDs (upper right), the light of which is collected by separate objective lenses for DIC and DRT. The side-on view (upper right) shows the inclined paths for the 3D-DIC measurement, which relay the specimen image to the upper and lower faces of a pyramid reflector. The top-down view (bottom-right) shows the splitting of the reflected light into two channels, which are recombined onto the left and right faces of the pyramid. The output image as recorded by a high-speed camera is shown in the bottom left.

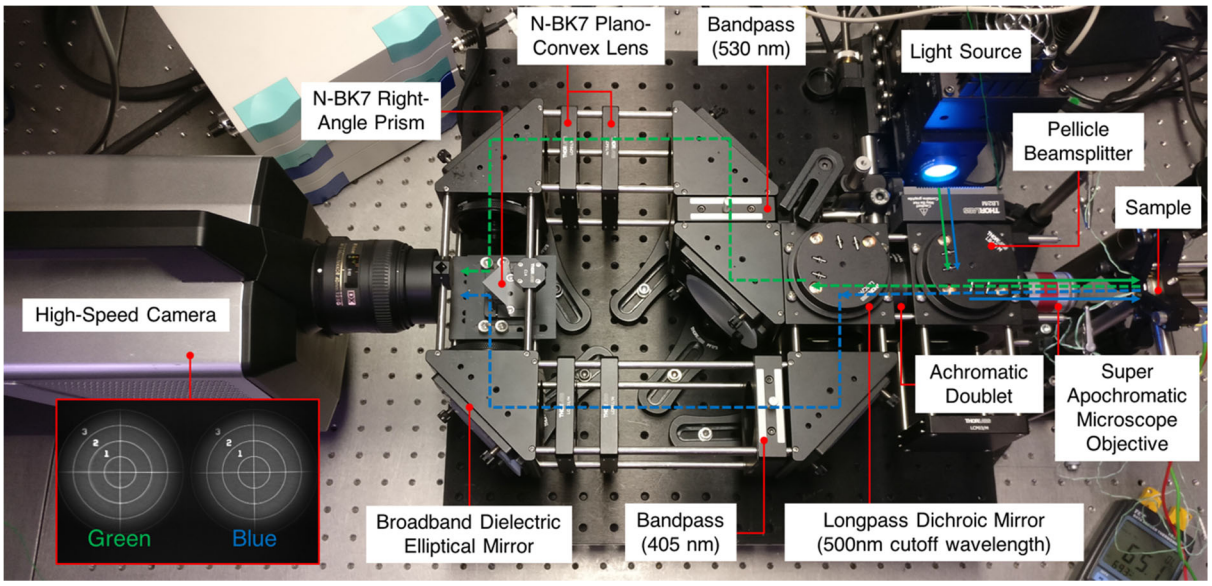

Figure 41. Experimental setup used to obtain full-field temperature measurements. This configuration replaces the doublet objective with a higher quality microscope objective to achieve increased magnification, and eliminates the separate DIC arms. Larger 2 inch optics as well as additional lenses between the objective and output image plane are also used to improve overall collection efficiency. Also shown in this setup is a Shimadzu HPV-X2 camera, which provides higher frame rates and resolution than the Phantom V7 used in the earlier setup.

3.6. Interpretation of Thermoreflectance Data

As described in the previous section, the surface of the specimen is illuminated with the two LEDs providing a narrow spectral emission band of light. The key assumption here is that the changes in reflectivity across the spectral emission band of *blue* light are not affected by temperature change. This is because the reflectivity of gold in this wavelength range is essentially temperature insensitive and there is less than 1% of change in reflectance up to 500°C [12]. Thus, only the specimen's tilt and surface changes might affect reflectivity measurements. The changes in reflectivity across the spectral emission band of *green* light are associated with changes in temperature [12] and, as in the case of *blue* light, are sensitive to the specimen's tilt and surface changes. This will be illustrated through a material characterization experiment, which was conducted for the purpose of model calibration (discussed later in the text).

Consider narrow spectral emission bands of *blue* and *green* light incident on a flat, smooth and gold-coated surface that experiences both a change in temperature and orientation. As shown in Fig. 42*Figure*, we separate these effects to occur at two distinct times, t_1 and t_2. We can write,

$$\mathcal{T}_0 < \mathcal{T}_1 = \mathcal{T}_2 \tag{1}$$

where $\mathcal{T}_0$ is the temperature at time t_i.

The reflectance of a surface is the ratio between the intensity of light reflected from a surface (I_R) and the intensity of incident light (I_I). Therefore, the change in reflectance (ΔR) between t_1 and t_0 can be expressed as,

$$\Delta R(\lambda, t) = \left.\frac{I_R(t_1)}{I_I(t_1)}\right|_\lambda - \left.\frac{I_R(t_0)}{I_I(t_0)}\right|_\lambda = \left.\frac{I_R(t_1) - I_R(t_0)}{I_I}\right|_\lambda, \tag{2}$$

where the illumination intensity at light wavelength λ is regarded as constant. Note that $\Delta R(\lambda, t) = 0$ when the reflectance is measured at the reference time, t_0. The relation between the relative change in reflectivity and the temperature change (ΔT) between times t_1 and t_0 can be expressed in terms of the thermoreflectance coefficient (κ) as,

$$\left.\frac{\Delta R(t_1)}{R_0}\right|_{\lambda_i} = \kappa_i \Delta T. \tag{3}$$

The value of κ is unique for each surface (material characteristics, chemical composition, etc.), and illumination wavelength, and must be known *a priori*. The temperature at the reference time t_0 should also be known and determined in advance. Note that κ over the range of 400–420 nm is very small ($\sim 1 \times 10^{-5} K^{-1}$), and thus there is no perceptible change in reflectivity across the spectral emission band of *blue* light. The corresponding change in reflectivity is less than 1% up to 500°C [12].

Next consider the case where the target surface orientation or roughness has changed at the time t_2, for this example represented by a tilt. In that case, we expect the reflected light to be modulated by a factor A, i.e.,

$$I_R^\star = A\, I_R, \tag{4}$$

where the □ is used to indicate the measurement in the tilted configuration. In the case of the *blue* channel, noting that the untilted reflected intensity is unchanged from the reference intensity, we can express this factor as,

$$A = \left.\frac{I_R^\star}{I_{R,0}}\right|_{\lambda_b}. \tag{5}$$

Both terms can be directly measured, and thus use of the *blue* channel allows us to correct for the effect of tilt in the reflected *green* channel. It follows that the corrected reflectance change for the *green* channel is,

$$\left.\frac{\Delta R}{R_0}\right|_{\lambda_g} = \left.\frac{I_R(t_0)}{I_R^\star(t_2)}\right|_{\lambda_b} \left.\frac{I_R^\star(t_2)}{I_R(t_0)}\right|_{\lambda_g} - 1. \tag{6}$$

The temperature change is then,

$$\Delta T = \frac{1}{\kappa_g}\left(\left.\frac{I_R(t_0)}{I_R^\star(t_2)}\right|_{\lambda_b} \left.\frac{I_R^\star(t_2)}{I_R(t_0)}\right|_{\lambda_g} - 1\right). \tag{7}$$

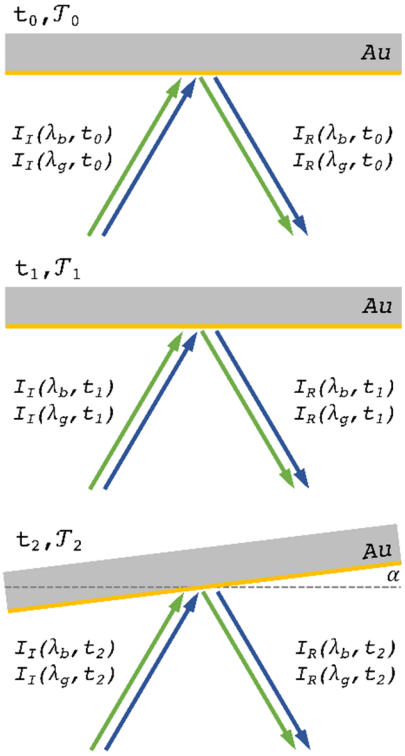

Figure 42. Basic concept of thermoreflectance imaging. The figure shows a flat, smooth and gold-coated surface that is illuminated with two incident light beams of narrow spectral emission bands of blue (λ_b) and green (λ_g) light, which have constant intensity (I_I) in time. Subfigures corresponds to: (top) gold-coated surface at reference temperature ($\mathcal{T}_0$) and time t_0; (middle) gold-coated surface that experienced the change in temperature ($\mathcal{T}_1$) at time, t_1; (bottom) gold-coated surface that experienced the change in reflectance angle at time t_2, and no change in temperature ($\mathcal{T}_2 = \mathcal{T}_1$).

Finally, the main concern of this approach and the related image analysis is to process the acquired images such that the correspondence of a single pixel (or small neighborhood around the pixel of interest) in one image can be found in the following images. This requires a pixel-to-pixel correlation between the images and also matching pixels from two imaging channels on the same image. This can be accomplished by the implementation of the DIC algorithms. As a result, a representative dataset is obtained, where each pixel point contains information on the light intensity in a discrete area of the specimen that was found in the *blue* and the *green* channel. This eventually allows to obtain the estimate of intensity (reflectance) change for each pixel and ultimately plot the temperature fields. Also, within the framework of this task, different averaging methods were explored to reduce the noise of post-processed images (Fig. 43), as well as algorithms for combining multiple images with similar fields of view.

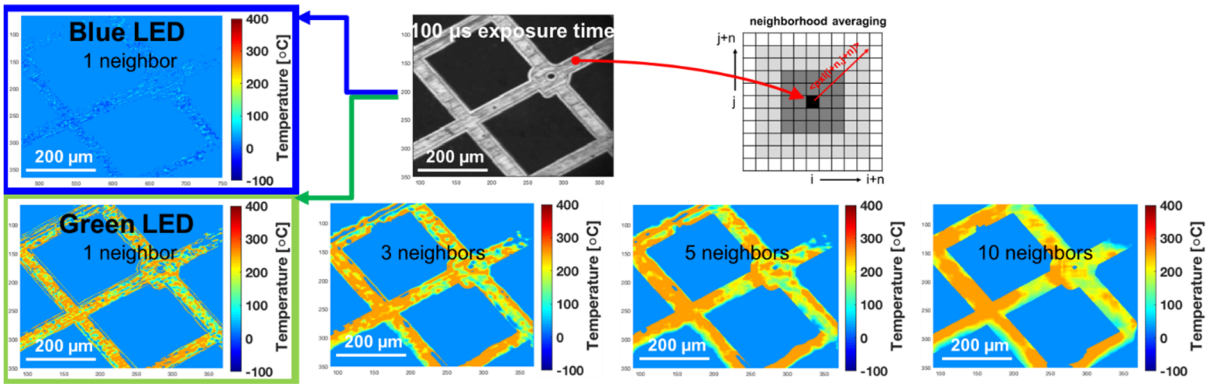

Figure 43. Post-acquisition image processing and filtering for noise reduction. A series of images (Green LED) shows an effect of spatial filtering (smoothing) on the full-field measurement of temperature. Here, the spatial filter modifies an image by averaging all of the pixels in neighbourhood around a central value (e.g., 3 neighbours – 3×3 area).

3.7. Experimental Validation

In this section, we present results from proof-of-concept experiments. As shown earlier, the DRT diagnostic comprises a significant number of optics, and thus requires an extensive validation to test requirements. For example, Fig. 44 shows a validation experiment illustrating the amount of light lost (or gained) due to the specimen's tilt and surface roughness. The object (a mirror in this case) was tilted ±5° such that the angle of incidence changed by ±5° (for 0° the light is incident close to normal). As the mirror rotates away from the normal axis, the amount of light collected by the objective lens drops rapidly. However, the reflectance ratio (ΔR) remains the same for both colour channels. This confirms that the system is well aligned and that the LED light sources are stable (pointing and intensity) over the duration of the measurement.

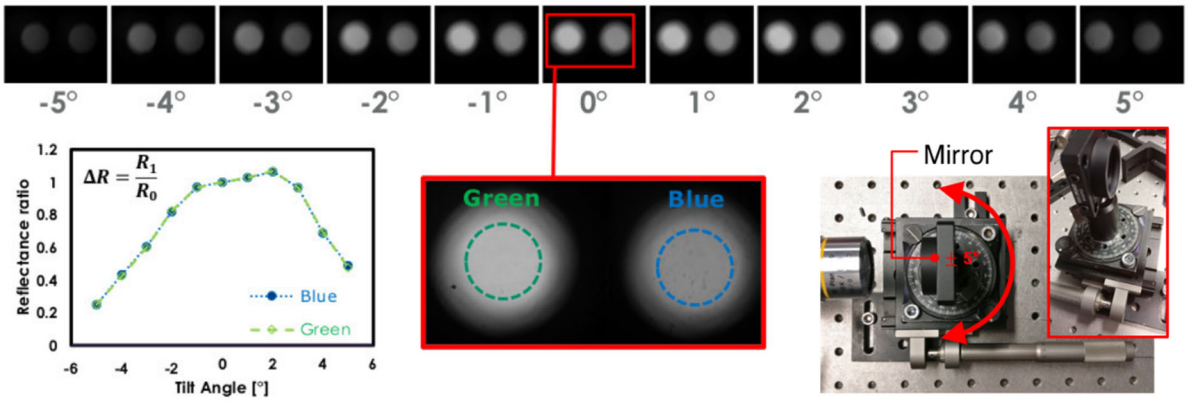

Figure 44. Experiment showing the change of reflectance with respect to the object's movement (translation and tilting) for the green and blue illumination. The image also shows the change of average reflectance ratio at non-normal angle of incidence for both channels.

The following two experiments illustrate the sensitivity of the DRT diagnostic to temperature change. As discussed earlier, the *blue* light is essentially temperature insensitive in the DRT measurements of gold. Thus, any change in reflectance observed during the tests occurs only because of changes in the specimen's tilt and surface roughness. The *green* light is used to measure the reflectance change related to the changes in temperature. Similarly to the previous case, this measurement is also

sensitive to the specimen's tilt and surface roughness. However, as shown in the previous experiment, the *blue* light can be used to monitor any non-temperature-related changes in reflectance, and compensate for these effects in the *green* channel.

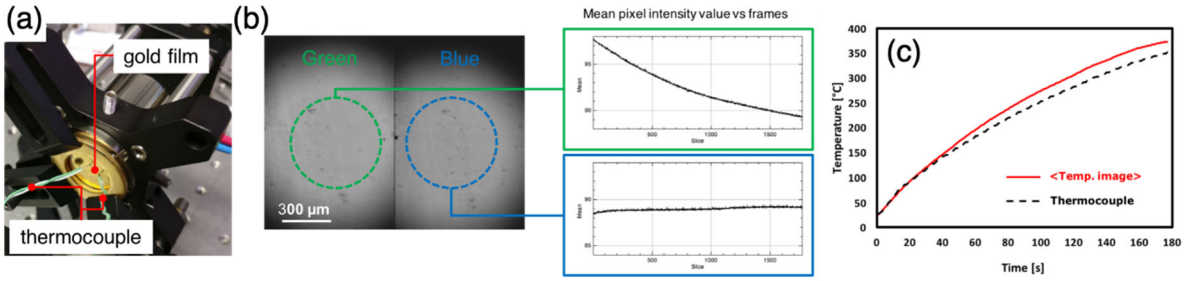

Figure 45. Experiment showing the change of reflectance with respect to the object's temperature, where: (a) experimental configuration (b) average of the pixel intensities within the encircled region show that the blue channel is temperature insensitive and the green channel is sensitive to the temperature change. (c) average temperature estimated based on the acquired images and measured with a thermocouple during the experiments.

Figure 45 shows the sensitivity of the DRT diagnostic to changes in temperature of a thin layer of gold. Here, a thin layer of gold was deposited on a sapphire window and heated up to elevated temperatures (25–350°C in 3min.). The reflectance change (in this case, drop in the light intensity) with rising temperature was observed for the *green* channel, while the *blue* channel maintained near constant light intensity during the whole experiment. The average temperatures estimated from the acquired images were compared to the temperatures measured with the thermocouple, and the numbers were found to be in good agreement (20°C of difference at 180°C). The difference between the two numbers was due to different locations of measurement points, i.e.: the thermocouple is located on the outside side of sapphire window (loss of surface heat via air conduction) and the DRT measurements are made on the inside side of sapphire window (closer to the heating stage).

Finally, a thin gold grid (~25 μm thick) was used as a target to demonstrate the capability of the DRT technique to obtain full-field measurements of temperature with high resolution photographs and short exposure times (Figure 46). The target was heated from room temperature to 250°C, and the images were acquired with a high-speed camera (Phantom v7.3) at 10fps, 640×480 pixel resolution, and 10 μs exposure time. It should be noted that the main challenge of the corresponding image analysis was to process the acquired images such that every pixel coordinate of the source images corresponds to the same location on the specimen in time. This required development and implementation of pixel-to-pixel correlation algorithms (stabilization of the acquired images) and matching pixels from two imaging channels (i.e., by overlapping two sets of images). The resulting dataset, where each pixel point contained information on the local temperature, is used to plot the estimated temperature fields. As in the previous experiments, the average temperature estimated from these images was close to the temperature measured by the thermocouple.

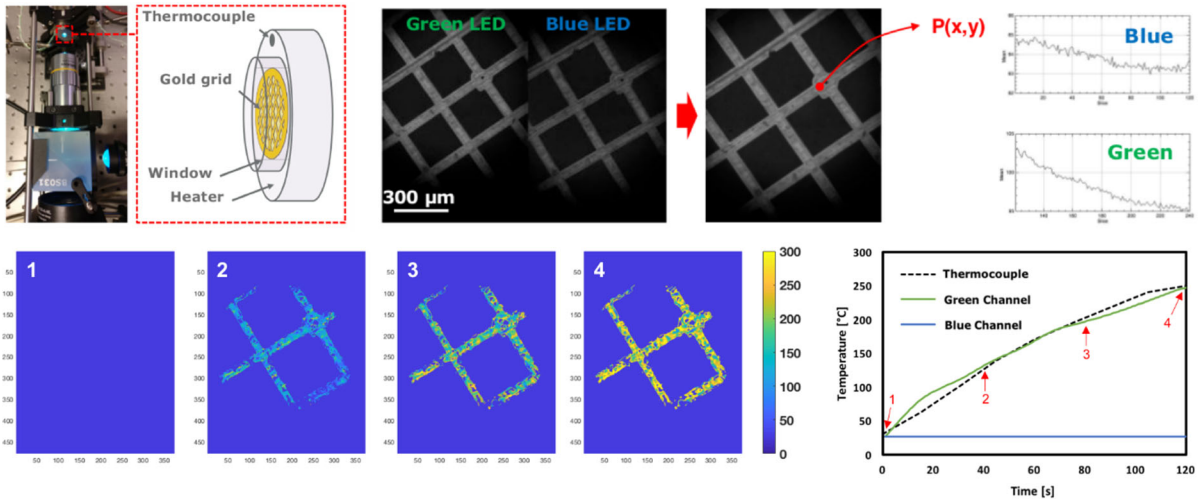

Figure 46. Experiment on a heated-up thin gold grid showing the image analysis procedure and corresponding full-field measurements of temperature. The image also presents an average temperature estimated based on the acquired images and measured with a thermocouple during the experiments.

3.8. Dynamic Temperature Measurements

In the final year of the program we attempted to measure the temperature of hot spots in heterogeneous energetic materials under confinement at high strain-rates. In these experiments, we used pure sucrose aggregates consisting of submillimetre-size grains as a model material system. The principle of the experiment (shown in Fig. 47) is as follows. First, a 200 mm long projectile is fired with a velocity of ~15 m/s towards the piston. Before the collision, the striker bar passes through a light gate and triggers two cameras at a predefined period of time. Camera 1 is focused on the end of the piston bar and records its displacement during the collision. The images are acquired at 30,000 fps, 320×240 pixel resolution, and 2 µs exposure time. Camera 2 is associated with the DRT diagnostics and acquires images of the back surface of the sapphire window. These images are acquired at 1000 fps, 400×250 pixel resolution, and 5 µs exposure time. Both cameras send frame rate sync signals to a digital oscilloscope, thus the compaction level of the sucrose aggregate can be correlated in time with the measurements of temperature. The sucrose aggregate is compacted against a 3 mm thick sapphire window, which is coated with a 150 nm layer of gold on one side. The experiment is designed such that the sucrose aggregate can be compacted up to 50% of its initial volume, but the level of compaction depends on the impact velocity and initial porosity of the aggregate.

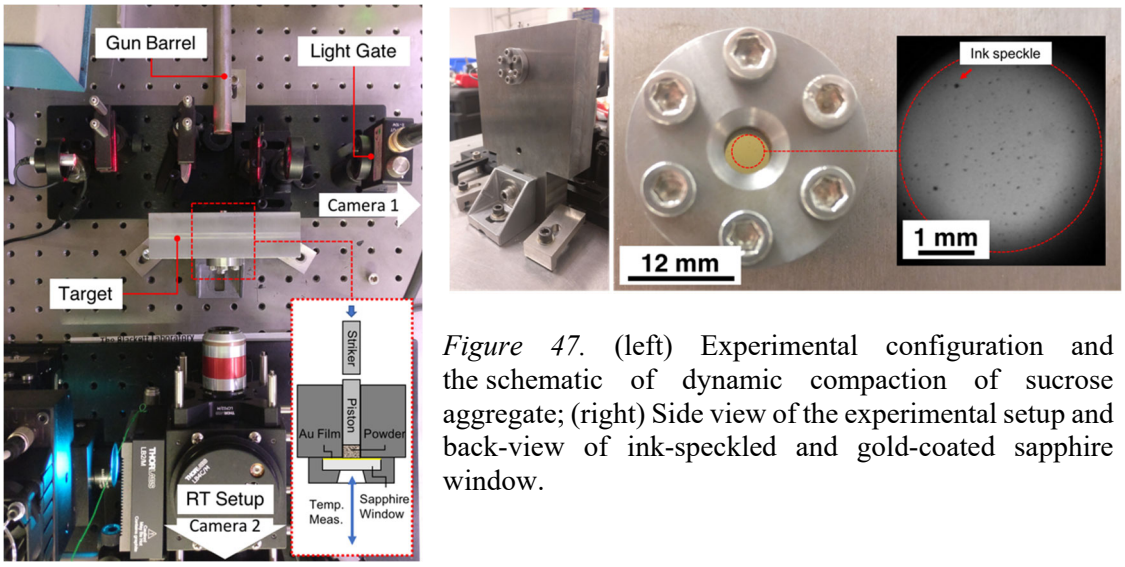

Figure 47. (left) Experimental configuration and the schematic of dynamic compaction of sucrose aggregate; (right) Side view of the experimental setup and back-view of ink-speckled and gold-coated sapphire window.

Figure 48 shows a sequence of images captured during the dynamic compaction of sucrose aggregate. The sapphire window was not gold coated in this experiment, thus the process of compaction can be observed with Camera 2. Three stages are presented, including (1) pre-compaction, where time 0 μs corresponds to the impact event, (2) first impact and the structure of the sucrose grains after the first impact, (3) second impact and the structure of the sucrose grains after the second impact. Note heterogeneous densification evolution of sucrose crystals, and the presence of coarse and fine aggregates in contact with the surface of sapphire window (indicated by the arrows in Fig. 48).

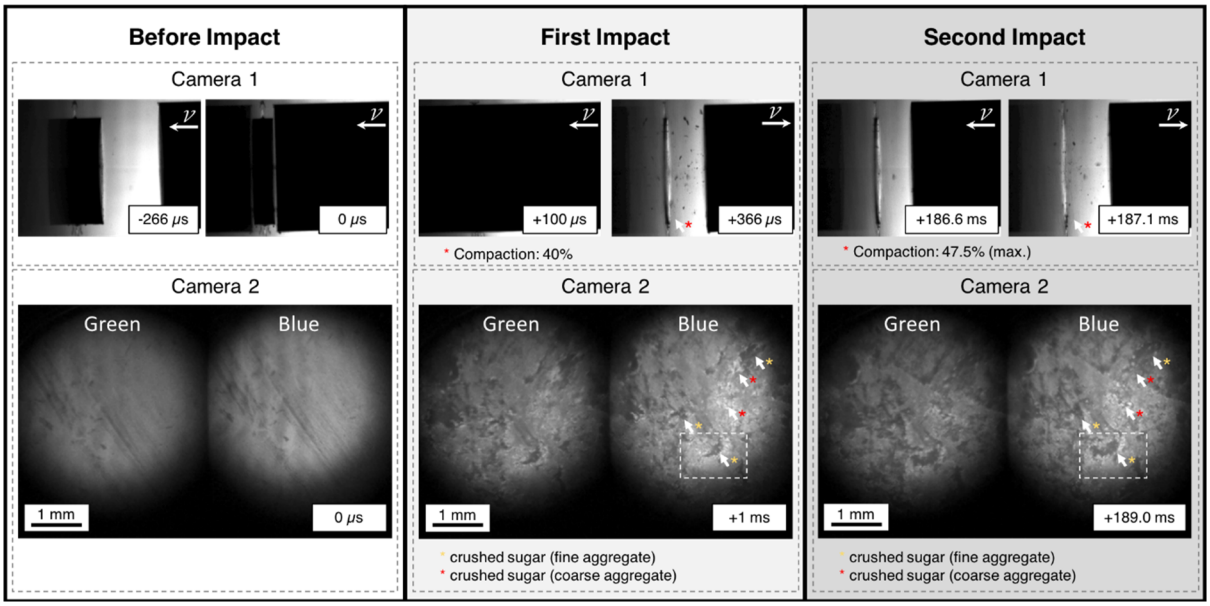

Figure 48. Dynamic compaction of sucrose aggregate (sapphire window without the gold sensor). Camera 1 visualizes the displacement of the piston bar during the collision. Camera 2 acquires images of the back surface of the sapphire window. The impact event is presented at three constitutive stages: (1) pre-compaction, where time 0 μs corresponds to the beginning of the impact event, (2) first impact and the structure of the sucrose grains after the first impact, (3) second impact and the structure of the sucrose grains after the second impact.

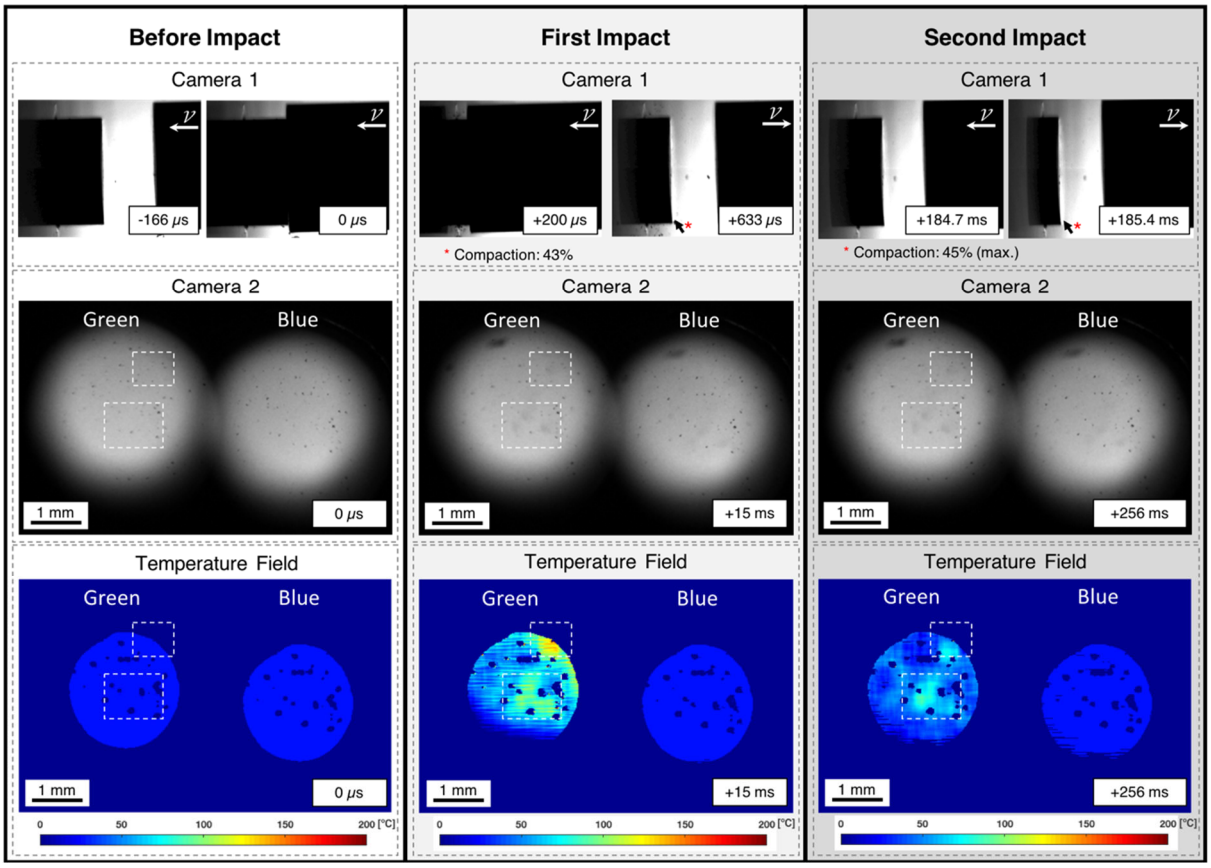

Figure 49. Dynamic compaction of sucrose crystals (sapphire window with the gold sensor) and the associated DRT analysis. Camera 1 visualizes the displacement of the piston bar during the collision. Camera 2 acquires images of the back surface of the sapphire window. The impact event is presented at three constitutive stages: (1) pre-compaction, where time 0 μs corresponds to the beginning of the impact event, (2) first impact and the structure of the sucrose grains after the first impact, (3) second impact and the structure of the sucrose grains after the second impact.

The first impact resulted in reduction of the volume of sucrose aggregate by 40%. The second impact led to further refinement of sucrose crystals, and consequently increased the area of contact between the fine aggregate and the sapphire window surface (e.g., area indicated by the white square in Fig. 48). After the second impact, the piston was completely seated within the steel block sample holder/confiner, and the overall compaction of sucrose aggregate increased to the maximum level of 47.5%.

Figure 49 shows an experiment with a gold coated sapphire window. The experimental conditions are the same as in the above-discussed case, and the presented impact stages corresponds to: (1) pre-compaction, where time 0 μs corresponds to the impact event, (2) first impact and the structure of the sucrose grains after the first impact, (3) second impact and the structure of the sucrose grains after the second impact. The following DRT analysis corresponds to the images captured by Camera 2 and shown in this figure. Note a substantial increase in the hot spot temperatures (up to 120°C). The locations of hot spots correspond to the dark features present on the gold sensor after the first impact (indicated by the white squares in Fig. 49). The change in the intensity of these pixels in both DRT-

related measurements (measurements that correspond to the *green* and *blue* channel, respectively) suggests that the physical and mechanical properties on the gold sensor have changed. These changes are likely induced by the crushing sucrose grains against the sapphire window, and can consequently be associated with the area of contact between the fine aggregate and the surface of sapphire window (as indicated by the white square in Fig. 48). Finally, the sucrose crystals before and after the test are presented in Fig. 50. The resulting heterogeneous structure and small indents present on the gold sensor confirm the above discussion. Figure 50 also shows the average estimated temperature during the impact events. Note that the temperature rise is perceptible during the impact events. However, the contribution of the gold sensor (the portion of plastic work converted into heat) to the measured temperature is unknown.

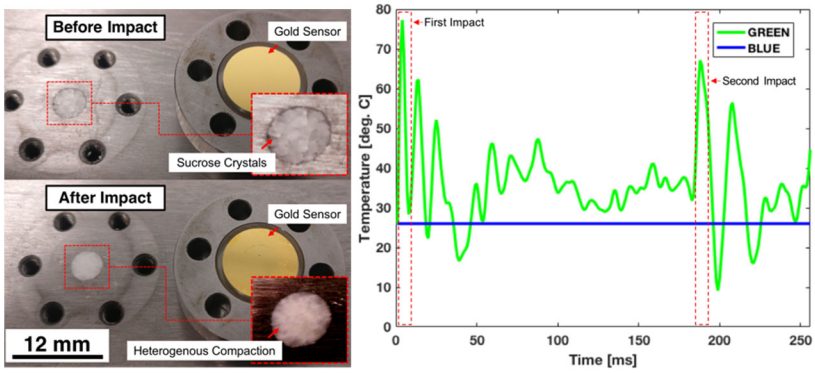

Figure 50. (Left) Sucrose aggregate before and after the test. The combination of fine and coarse grains in the recovered material shows evidence of heterogeneous compaction. (Right) Average temperature in the area of interest as measured using the DRT technique. The high time resolution enables capture of signatures of the initial and secondary impact.

3.9. Conclusions and Directions for Future Work

A DRT diagnostic tool has been developed for simultaneous high-speed measurements of temperature and deformation fields in HEMs during dynamic loading condition. This experimental approach combines the state-of-the-art high-speed camera technologies and visible light thermoreflectance technique supported by single-colour ultra-high brightness LEDs that produce narrow spectral emission bands of *blue* and *green* light. Within the framework of this program, the broad scope of work was completed and these cover the following research topics:

(1) Exploration of different laser-based illumination sources that could be potentially used in DRT measurements. For example, a significant amount of time was dedicated to the solid-state laser diodes due to their highly directional output, ease of propagation and focusing using standard optics. We reported that the lasers introduce additional challenges as their coherence results in undesirable spatial modulations in intensity (speckle) at the image plane. We tried to minimise the speckle effect using the following approaches: (i) wavelength diversity by combining the output from several slightly detuned lasers, (ii) polarization diversity by using light with different polarization from several slightly detuned lasers, (iii) angle diversity by illuminating the specimen under different incident angles of light, (iv) using diffusers (static and moving), (v) fibre-based coupling and mixing of the output light from several lasers, (vi) optical path length modulation (vibrating fibres), and (vii) combination of two or more methods above mentioned. The obtained results were not completely satisfactory and the

further work was focused on the LED technology that produce narrow spectral emission bands of *blue* and *green* light.

(2) Characterisation of the optical properties of gold sensors as prepared on target surfaces of various roughness (discussed in a 1st Year Progress Report). Despite the fact that in our final experiments we used gold sensors on highly polish optical windows, the exploration of other quality surfaces or direct application of gold sensors on HEMs was an important part of this program. For example, we found that the deposition of gold sensors on highly polished surfaces might cause additional challenges in temperature measurements associated with redirection of collimated light or delamination of gold sensors under large deformations. Local deviations of a surface from a perfectly flat interface can improve the adhesion behaviour of gold/HEMs interfaces and survivability of gold sensors during large deformations. This is because the complex geometry of a contact surface can help to match locally the strain levels in the gold sensor and HEMs. The surface texture can also improve the reliability of collected signals when performing the DRT measurements with collimated light sources during large deformation.

(3) Demonstration of surface strain and temperature measurements under high strain-rate loading (not included in our reports). We performed simultaneous measurements of local surface strains (2D DIC) and temperature fields on titanium alloy specimens under dynamic shear loading conditions. The DRT measurements were performed with resolutions below 5 microns in space and 1 microsecond in time.

(4) Post-processing of the acquired images was an important part of the data analysis process. This required development of new tools for image processing and image manipulation, which allowed to obtain full-field temperature measurements in a repeatable way and with a low level of uncertainty.

(5) Demonstration measurements of non-uniform thermal landscapes (hot spots) in HEMs under dynamic loading conditions.

Although the AFSOR program is coming to an end, we will continue our research activities and address the following needs:

1. Engage the experimental capabilities established at GeorgiaTech and Imperial College London in a combined experimental campaign. Particularly, we are planning to perform a series of identical dynamic experiments on HEMs with (1) simultaneous high-speed IR and VL imaging at GeorgiaTech and (2) simultaneous high-speed DRT and VL imaging at Imperial College London. As a result, we will demonstrate how our research developments can be integrated with each other, so that the dynamic thermo-mechanical properties of HEMs can be resolved at different time-scales and length scales.

2. Explore Au thin-film patterning methods to deposit e.g. grids or patches. This would serve to eliminate the need for ink speckle for the DIC technique, as well as limit lateral thermal conduction through the Au film.

3. Conduct DRT measurements during plate-impact loading of HEMs. This will be a natural extension of our dynamic compaction of sucrose aggregate tests to very high strain-rate.

4. Identify the most suitable camera for high-speed DRT measurements. We learn over the course of the program that the camera with high sensitivity and low noise is essential for DRT measurements. Also, most of high-speed cameras have a tradeoff between high spatial and high temporal resolutions, and this tradeoff limits their use in DRT measurements during plate-impact loading of HEMs.

4. Publications and presentations

(1) Z. Kang, A. A. Banishev, G. Lee, D. A. Scripka, J. Breidenich, P. Xiao, J. Christensen, M. Zhou, C. J. Summers, D. D. Dlott, and N. N. Thadhani, Exploration of CdTe quantum dots as mesoscale pressure sensors using time-resolved shock-compression spectroscopy, *Journal of Applied Physics*, **120**, 043107, 2016.

(2) S. Kim C. Miller, Y. Horie, C. Molek, E. Welle, and M. Zhou, Computational Prediction of Probabilistic Ignition Threshold of Pressed Granular HMX under Shock Loading, *Journal of Applied Physics*, **120**, 115902, 2016.

(3) P. Xiao, Z. Kang, A. A. Bansihev, J. Breidenich, D. A. Scripka, J. Christensen, C. J. Summers, D. D. Dlott, N. N. Thadhani and M. Zhou, Laser-excited Optical emission response of CdTe quantum dot/polymer nanocomposite under shock compression, *Applied Physics Letters* **108**, 011908, 2016.

(4) David Scripka, Garrett LeCroy, Christopher J. Summers, Naresh N. Thadhani, Spectral response of multilayer optical structures to dynamic mechanical loading, Appl. Phys. Letters, 2015.

(5) David Scripka, Gyuhyon Lee, Garrett LeCroy, Zhitao Kang, Christopher J. Summers, Naresh N. Thadhani, Experimental and computational Analysis of spectral response of multilayer optical structures to laser shock loading, J. of Applied Phys., 2015.

(6) G. Lee, D.A. Scripka, B. Wagner, N.N. Thadhani, Z. Kang, C.J. Summers, Optics express 25 (22), 27067-27076, 2017.

(7) D Scripka, G LeCroy, G Lee, C Sun, Z Kang, CJ Summers, NN Thadhani, Spectral response of multilayer optical structures to dynamic loading, AIP Conference Proceedings 1793 (1), 060006, 2017.

(8) D. Scripka, G. Lee, Z. Kang, C.J Summers, and N.N. Thadhani, Time-resolved spectral response of asymmetrical optical microcavity structures under laser-driven shock compression, AIP Advances, 15021 (2018).

(9) A. Keyhani, R. Yang, and M. Zhou, Novel Capability for Microscale In-situ Imaging of Temperature and Deformation Fields under Dynamic Loading. Experimental Mechanics. 2019:1-6.

(10) C. Miller, S. Kim, Y. Horie, and M. Zhou, Ignition thresholds of aluminized HMX-based polymer-bonded explosives, AIP Advances **9**, 045103, 2019.

(11) U. Roy, S. Kim, C. Miller, Y. Horie, and M. Zhou, Computational Study of Ignition Behavior and Hotspot Dynamics of a Potential Class of Aluminized Explosives, Modelling and Simulation in Materials Science and Engineering **26**, 085004, 2018.

(12) Y. Wei, S. Kim, Y. Horie, and M. Zhou, Quantification of Shock Initiation Thresholds and Ignition Probability of Polymer-Bonded Explosives with Initial Defects, Journal of Applied Physics **124**, 165110, 2018.

(13) S. Kim, Y. Wei, Y. Horie, and M. Zhou, Prediction of Shock Initiation Thresholds and Ignition Probability of Polymer-Bonded Explosives using Mesoscale Simulations, Journal of the Mechanics and Physics of Solids **114**, 97-116, 2018.
(14) L. Farbaniec, D.E. Eakins, "LED-based thermoreflectance diagnostic for full-field temperature measurements in dynamic experiments", (In preparation).
(15) L. Farbaniec, D.E. Eakins, "Speckle contrast reduction in laser-based illumination system for dynamic temperature measurements by means of thermoreflectance technique", (In preparation).
(16) L. Farbaniec, D.J. Chapman, M. Zhou, D.E. Eakins "Adiabatic shear localization and thermal softening in hexagonal close-packed metals under high strain-rate loading", (In preparation)

Presentations: (♦ denotes invited talk, invited keynote talk, invited plenary lecture, invited lecture, or invited seminar)

(1) Meso-scale diagnostics and modeling for temperature and deformation fields in heterogeneous energetic materials, Triservice Energetic Materials Programs Review, August 15, 2016, Arlington, VA;
(2) Design of heterogeneous materials: determination of macroscopic properties from microscopic attributes, International Symposium on Heterogeneous Materials Mechanics, Chongqing University, Chongqing, China, June 8-10, 2016; ♦
(3) 2nd Joint Sandia-Georgia Tech Materials Workshop, Sandia National Labs, February 10-11, 2016, Albuquerque, NM, Prediction of Fracture Toughness and Ignition Threshold from Microstructure-level Simulations and Measurement of Deformation and Temperature Fields at Mesoscale under Dynamic Conditions; ♦
(4) Meso-Scale Simulations and Time-Resolved Diagnostics for Understanding Shock Compression Response of Reactive Powder Mixtures, University of Michigan, Ann Arbor, 2016♦
(5) Multilayer Optical Structures fir Time-resolved sensing of heterogeneous effects during shock compression, Institute of Mechanics, Beijing, China, 2016.♦
(6) Meso-Scale Sensing of Shock Compression Effects in Heterogeneous Materials, Arizona State University, 2017. ♦
(7) Multilayer Optical Structures for Time-Resolved Meso-Scale Sensing Of Shock Compression Effects In Heterogeneous Materials, ICMRE Conference, Beijing, China, 2017. ♦
(8) Multilayer Optical Structures For Time-Resolved Meso-Scale Sensing Of Shock Compression Effects In Heterogeneous Materials, AFRL Eglin Air Force Base, September 28, 2017.
(9) Microstructure Effects on Dynamic Tensile (Spall) Strength of Titanium-based Bulk Metallic Glass and its Composites, MS&T Conference, Pittsburgh, October 9, 2017
(10) Time-Resolved Optomechanical Sensing Of Pressure Distributions During Shock-Compression Of Heterogeneous Materials, MATSE Colloquium, University of Illinois at Urbana-Champaign, February 12, 2018.
(11) Time-Resolved Optomechanical Sensing Of Pressure Distributions During Shock-Compression Of Heterogeneous Materials, 2018 MACH Conference, Annapolis, MD, March 2018.
(12) L. Farbaniec, J. Patten, D. Chapman, D. Eakins "Implementation of a laser-based thermoreflectance diagnostic for full-field temperature measurements in SHPB experiments", Dymat 23rd Technical Meeting, 12–14 September 2017, Trondheim, Norway.

(13) L. Farbaniec, J.R.W. Patten, T. White, D.E. Eakins "Thermomechanical characterisation of shear localisation during high-rate loading", 2nd International Workshop on Mechanistic Behaviour of HCP Alloys, 5 April 2018, London, UK.
(14) L. Farbaniec, J.R.W. Patten, T. White, D.E. Eakins "Dynamic behaviour of Ti-6Al-4V alloy under high strain-rate loading", 2nd International Workshop on Mechanistic Behaviour of HCP Alloys, 17–19 September 2018, Oxford, UK.
(15) L. Farbaniec, A. Keyhani, D.J. Chapman, M. Zhou, D.E. Eakins "Novel meso-scale diagnostics for temperature and deformation field measurements in energetic materials", 2019 Mach Conference, 3–5 April 2019, Annapolis, USA
(16) L. Farbaniec, D.J. Chapman, M. Zhou, D.E. Eakins "Adiabatic shear localization and thermal softening in hexagonal close-packed metals under high strain-rate loading", 2019 Mach Conference, 3–5 April 2019, Annapolis, USA
(17) L. Farbaniec, D.E. Eakins "Thermomechanical properties of hexagonal close-packed metals under high strain-rate loading: a novel approach to diagnostic and full-field measurements of temperature and strain fields", the 24th DYMAT Technical Meeting "Temperature dependence of material behaviour at high strain-rate", 9–11 September 2019, Stresa, Italy (accepted)
(18) Microscale In-situ High-speed Imaging of Temperature and Deformation Fields, 21st Biennial Conference of the APS Topical Group on Shock Compression of Condensed Matter (SHOCK19), June 16-21, 2019, Portland, Oregon.
(19) Microstructure effects on safety, reliability, and performance of energetic materials, Army Workshop on Encapsulated Trigger-Release Chemistry for Sustainable End of Life Cycle Product Management, April 9-10, 2019, University of Rhode Island, West Greenwich, RI. ♦
(20) Novel Capability for Microscale In-situ Imaging of Temperature and Deformation Fields under Dynamic Loading, Mach Conference, April 3-5, 2019, Annapolis, MD. ♦
(21) Influence of Chemistry in HMX-based PBX Initiation, 16th International Detonation Symposium, Cambridge, MD, July 15-20, 2018. ♦
(22) High-speed Measurement of Temperature, Deformation, and Stress Fields at the Microstructure Level, March 20, 2018, Sichuan University, Chengdu, China. ♦

5. New discoveries, inventions, or patent disclosures

(1) M. Zhou, A. Keyhani, and R. Yang, Microscale In-situ Imaging of Dynamic Temperature and Deformation Fields (MINTED), GTRC ID 8064, December 12, 2018. Provisional U.S. Patent Application # 62/795,339, January 22, 2019.

6. Collaborations and Transitions

We have been working with Drs. Eric Welle and Tom Kostas at the Eglin AFB in Florida in the development of simulant samples for experiments using Melanie and sugar. We have also been working with the Telops Inc. in Quebec, Canada on the development of custom IR optics for combined IR and VL measurements.

7. Personnel Supported

Graduate students, postdocs, and visiting scholars:

Amirreza Keyhani (GT)
Dr. Rong Yang (GT)
David Scripka (GT)
Andrew Boddorff (GT)
Gyuhyon Lee (GT)
Dr. Greg Kennedy (GT)
Dr. Lukasz Farbaniec (ICL)

References

1. Ramos, K. and D. Bahr, *Mechanical behavior assessment of sucrose using nanoindentation.* Journal of materials research, 2007. **22**(7): p. 2037-2045.
2. Hardman, J. and B. Lilley, *Deformation of particles during briquetting.* Nature, 1970. **228**(5269): p. 353.
3. Huffine, C.L., *A study of the bonding and cohesion achieved in the compression of particulate materials*. 1953, Columbia University 1953.
4. Bridgman, P.W., *Physics of high pressure.* 1952.
5. Blaber, J., B. Adair, and A. Antoniou, *Ncorr: Open-Source 2D Digital Image Correlation Matlab Software.* Experimental Mechanics, 2015. **55**(6): p. 1105-1122.
6. Keyhani, A., et al., *Energy Dissipation in Polymer-Bonded Explosives with Various Levels of Constituent Plasticity and Internal Friction.* Computational Materials Science, 2018. **159**: p. 136-149.
7. Scripka, D., et al., *Spectral response of multilayer optical structures to dynamic mechanical loading.* Applied Physics Letters, 2015. **106**(20): p. 201906.
8. Xu, X., et al., *The study on the interface adhesion comparison of the MgF 2, Al 2 O 3, SiO 2 and Ag thin films.* Applied surface science, 2005. **245**(1): p. 11-15.
9. Brown, K.E., et al., *Time-resolved emission of dye probes in a shock-compressed polymer.* Journal of Applied Physics, 2012. **112**(10): p. 103508.
10. Setchell, R.E., *Index of refraction of shock-compressed fused silica and sapphire.* Journal of Applied Physics, 1979. **50**(12): p. 8186-8192.
11. Dolan, D.H., T. Ao, and C.T. Seagle. *Reflectance thermometry in dynamic compression experiments*. in *AIP Conference Proceedings*. 2013. AIP.
12. Dolan, D.H., C.T. Seagle, and T. Ao, *Dynamic temperature measurements with embedded optical sensors.* SANDIA Report No. SAND2013-8203, 2013.